ORIGINAL PAPER

Linkages between Madden–Julian oscillation and drought events over Kenya

Phillip Okello Ochieng[1,2] · Isaiah Nyandega[1] · Boniface Wambua[1] · Victor Ongoma[3]

Abstract

Increased frequencies and intensities of extreme weather events have negatively impacted climate-sensitive socio-economic sectors in Kenya and larger Equatorial East Africa (EEA). Madden–Julian oscillation (MJO) influence intra-seasonal weather variability over Kenya although less attention has been given to its effect on extreme weather events such as droughts and floods, which have increased in frequency and intensity. Outgoing Longwave Radiation (OLR) was used in this work as proxy data for rainfall to study the geographical distribution and circulation anomalies associated with MJOs and their impacts on extreme weather events. Extreme weather events are identified using the self-calibrating Palmer Drought Severity Index (sc-PDSI), based on sc-PDSI, 2013/2014 and 2017/2018 as the drought and flood years, respectively. The background power spectral analysis reveals that MJOs are more dominant during the March–May (MAM) season than other seasons. The variance analysis depicted that the maximum power of MJO-filtered OLR is cantered within the tropical Indian Ocean, maritime continent and the tropical Pacific Ocean. Upper tropospheric (200 hPa) wind signatures give a clear Matsuno-Gill-type circulation compared to the lower tropospheric wind flows. Thus, the signatures can be used to develop a dynamic MJO index for prediction purposes. There exists a weak direct relationship between MJO and sc-PDSI; however, the influence may result from its modulation of atmospheric circulation as illustrated by the wind and velocity potential patterns before and after the passage of the convective MJO phase.

1 Introduction

Extreme weather events such as droughts and floods have far-reaching consequences on the economy and the environment at large (Seneviratne et al. 2012; Lyon 2014; Basu et al. 2016). Although the occurrence of droughts is inevitable, a lot can be done to minimize the associated negative impacts. The measures may include but are not limited to an early warning system that enhances preparedness for sustainable adaptation and mitigation actions (Kilavi et al. 2018). Drought forecasting forms a fundamental component of the

drought early warning system by adopting better forecasting methods.

Arid and Semi-Arid Lands (ASALs) in Kenya are the most prone and vulnerable to droughts. Unlike other meteorological hazards experienced in these regions (e.g., flash floods, landslides), drought events are more devastating since they exacerbate the water scarcity condition. The over-dependency of the local community on pastoralism which relies on rain-fed pastures as the main economic activity further aggravates this situation. The 2008–2010 drought, for example, affected the entire East Africa region, with approximately 13 million people directly impacted (Muller 2014). Pastoralists lost over 60 percent of their livestock (Huho and Kosonei 2014); an estimated 3.2 million people in ASALs of Kenya were left in need of emergency help. The drought situation that used to occur after every 5 years has become more frequent and intense, and its management has been complicated by other pandemics such as COVID-19 (Funk 2020).

The rainfall pattern in Kenya is characterized by two maxima experienced during October to November (OND) and March to May (MAM), locally referred to as 'short'

✉ Phillip Okello Ochieng
    koderaphillips@yahoo.com

1   Department of Earth and Climate Sciences, University of Nairobi, P.O. Box 30197-00100, Nairobi, Kenya

2   Kenya Meteorological Services, P.O. Box 30259-00100, Nairobi, Kenya

3   Mohammed VI Polytechnic University, Lot 660, Hay Moulay Rachid, 43150 Ben Guerir, Morocco

and 'long' rains, respectively (Okello et al. 2021). At numerous temporal and geographical dimensions, many factors govern the start, length, and rebound from climate extremes, especially floods and droughts (Frei et al. 2006; Dai 2013; Sun et al. 2016). In particular, teleconnections such El Nino–Southern Oscillation (ENSO), Madden Julian Oscillations (MJO), the North Atlantic Oscillation (NAO), the Indian Ocean Dipole (IOD), and the Pacific Decadal Oscillation (PDO) have a substantial impact on climatic extremes (Weisheimer et al. 2017; Zhang et al. 2010). For instance, the positive and negative phases of ENSO are associated with above and below-normal rainfall, respectively, over East Africa OND (Omondi et al. 2014; Indeje et al. 2000b; Kalisa et al. 2020; Mpelasoka et al. 2018).

The IOD is the primary influencer of rainfall variability over Kenya throughout the MAM season (Mpelasoka et al. 2018; Ongoma et al. 2015; Owiti et al. 2008). Warming (cooling) in the western Indian Ocean is connected with a positive (negative) phase of the IOD. The positive phase of IOD is associated with enhanced rainfall in Equatorial East Africa (EEA).

Madden–Julian Oscillation (MJO, a 30- to 60-day oscillation) is one of the most important features that influence climate variability within the tropics (Zhang 2005). It is known to cause intra-seasonal to seasonal rainfall variability in Kenya (Hogan et al. 2015; Omeny et al. 2008; Pohl and Camberlin 2006). The Indian Ocean, the Caribbean, the Pacific Ocean and Africa are all affected by this belt of deep convective clouds moving eastward at a speed of about 5 miles per hour (8.0 km/h). According to Madden and Julian (1994), the MJO is strongest in the winter and weakest in the summer, even though it is present year-round. Although its strength varies seasonally, it impacts climate and weather events all year round in the tropics and extra-tropics. MJO is also known to have a considerable impact on the atmospheric circulation in the global tropics, as well as causing fluctuations in the weather and temperature in non-tropical places around the world (Bond and Vecchi 2003; Zhang 2005).

Zhang (2005) provided a comprehensive study of the MJO's properties and dynamics. Similar studies have been done by Li (2014), and Demott et al. (2015). A convective core that is made up of a large number of small-scale deep convective structures is what distinguishes the "active phase" of the MJO from other phases. Near the surface, zonal winds blow in the same direction as the core, but higher up, they are blowing in opposite directions. Active phase convergence is seamlessly connected to a "suppressed phase" of low convection and surface divergence that flows along with the active phase. This results in the production of a convective dipole that can traverse significant areas of the world's tropical regions. Large-scale tropospheric heating that is linked with the active phase of the MJO is what

typically leads to eastward-propagating dry Equatorial Kelvin waves and westward-propagating Equatorial Rossby Waves.

In Kenya, MJO influence on extreme weather events, which could be vital information for the prediction of inter-seasonal rainfall in East Africa (Kimani et al. 2020; Kilavi et al. 2018; Omeny et al. 2008). There is a correlation between the MJO's influence on precipitation and its modulation of large-scale tropospheric circulation, oscillating between favourable and unfavourable circumstances for upward vertical movement and convection (Schreck et al. 2013). Mutai and Ward (2000) observed that a form of intraseasonal rainfall variability in EEA short rains corresponds to MJO timeframes. They determined that intensified MJO convection in the Indian Ocean lags positive rainfall anomalies by about 5 days. As this link is time-lagged, Mutai and Ward (2000) indicate that EEA convection may lead to the generation of MJO episodes in the Indian Ocean. However, they did not study the processes by which the MJO influences EEA precipitation, but they did underline the vital implications of scale interlinks between intra-seasonal oscillations, including the MJO, and inter-annual climatic variability impacting EEA precipitation.

Omeny et al. (2008) quantified the relationships between MJO and precipitation over Kenya. Similar to Pohl and Camberlin (2006), they reported a substantial association between highland rainfall, in this instance rainfall in western Kenya, and MJO when the MJO convective core is in the Indian Ocean. When the MJO advances into the Western Pacific, rainfall in western Kenya decreases. The outcome is the same for both short and long rains. The study highlights that this link might be used to inform 10-day-ahead rainfall estimates, but it advocates for integrating MJO information with other diagnostics to account for a larger proportion of variability. Omeny et al. (2008) observed insignificant relationships between the MJO and precipitation in eastern Kenya.

Berhane and Zaitchik (2014) extend the research of Pohl and Camberlin (2006) and Omeny et al. (2008) by analysing sub-seasonal variation in the MJO's contribution on EEA during both the short and long rainy seasons. They found that MJO convection in the Indian Ocean is related to increased EEA highland rainfall throughout the long rains, but that the association is strongest near the conclusion of the MAM season. During the short rains, substantial connections with highland precipitation are weaker in October than in November and December. In October, however, there is a strong negative relationship between Maritime Continent MJO convection and coastal EEA precipitation that is absent later in the season.

Extreme drought research has gained a lot of research interest on the international scene. Understanding the dynamic dynamics behind extreme drought occurrences

has not yet been established. The catastrophic droughts have affected Kenya in the recent past and are projected to persist into the future over most parts of East Africa (Haile et al. 2020). There is a great deal of scientific value in investigating and uncovering the reasons behind these incidences. This study's findings may help improve present monitoring and prediction technologies for catastrophic climate occurrences like Kenya's droughts. As mentioned earlier, larger-scale atmospheric and oceanic variability effects and modulates all processes. All of this prior research has focused on the effects of the MJO on either rainfall over the study region. However, the effects of MJO droughts on floods have been rarely investigated over the study area. This research aims at finding the effects of the tropical MJO on this bimodal rainfall pattern and examine the physical factors for the occurrence of drought events in terms of the persistent intra-seasonal atmospheric circulation anomalies in the MJO, as well as to provide scientific evidence for the monitoring and prediction of extreme droughts and floods through establishing the nexus between MJO and drought.

2 Data and methodology

2.1 Study area

Kenya lies between longitude 34° E and 42° E and latitude 5° S and 5° N (Fig. 1). The country is surrounded by Uganda, Ethiopia, Tanzania, Southern Sudan and Somalia. The country's economy and most households are largely dependent on rain-fed agriculture (Eichsteller et al. 2022). The central highlands have the highest elevation, whereas the climate and natural systems of the low-lying eastern, northwest, and north-eastern parts are mainly ASAL. The average annual precipitation ranges from less than 250 mm in the ASALs to more than 2000 mm in regions with high potential (Ochieng et al. 2022). The Indian Ocean to the south regulates the local climate pattern of the adjacent coastal zones, but the enormous water basin of Lake Victoria on the western flanks of the research area drives land-lake breezes with modifying the climate of its basin (Okoola 1999).

Fig. 1 Digital elevation map and the location of the study area **a** Kenya **b** Africa and **c** Eastern Africa. Data represents the Shuttle Radar Topography Mission (SRTM) 30 m image for Kenya. These SRTM was created through mosaicking tiles and clipping to the extent of the country. The digital elevation and major lakes were mapped using the shapefiles obtained from the World Resources Institute (WRI) (National Space Agency et al. 2000)
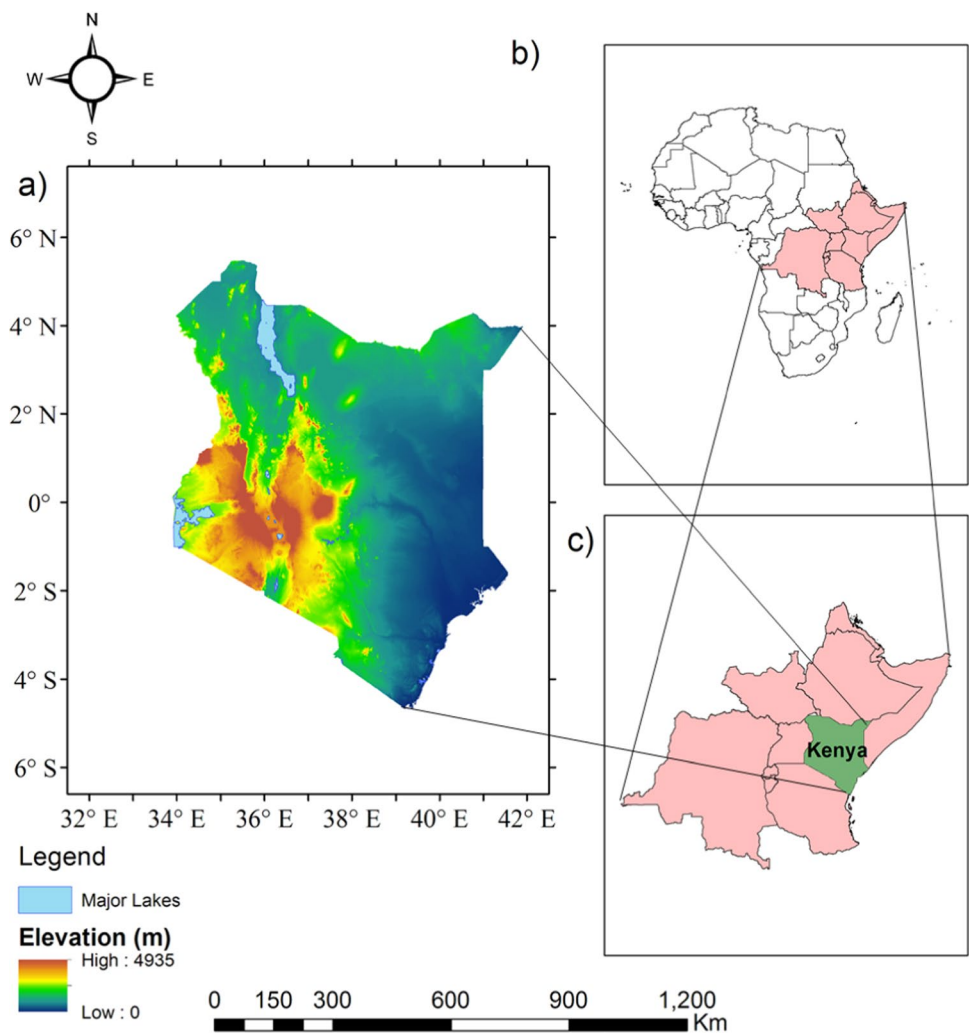
Owiti et al. (2008) conducted extensive research on Kenya's annual rainfall cycle, while most studies (e.g., Indeje et al. 2000b; Ogwang et al. 2015; Okello et al. 2021) focused on rainfall over the larger East Africa region. The studies found that the first and second maxima of precipitation occur in MAM and OND, respectively, in these geographical areas. The minimum rainfall is recorded during December–February (DJF) and June–August (JJA). The meridional and zonal propagation of the ITCZ (convective rainfall belt) is mainly responsible for this rainfall seasonality (Camberlin et al. 2001; Ongoma et al. 2015; Nicholson 2018). Droughts across Kenya and the wider EEA region are complex phenomena involving multiple teleconnection mechanisms. There is evidence that the ENSO is responsible for some of the extreme weather in East Africa (Indeje et al. 2000a; Kalisa et al. 2020; Lyon 2014; Masih et al. 2014).

2.2 Data

This study utilized a monthly gridded temperature dataset for the computation and modification of the projected Thornthwaite Evapotranspiration. The data has a spatial resolution of $0.5° \times 0.5°$, sourced from the Climatic Research Unit, CRUTS4.03 (Harris et al. 2014). CRU temperature dataset has successfully been applied by Polong et al. (2019) in the computation of potential evapotranspiration (PET) over the Tana River basin, Kenya. Similarly, Ayugi et al. (2020) successfully utilized the data to calculate PET in their evaluation of drought over Kenya based on SPEI.

Climate Hazard Group Infrared Precipitation with Station monthly precipitation datasets (CHIRPS v2; Funk et al. 2015) was used in the computation of sc-PDSI. The spatial resolution of the CHIRPS data package is 0.05 (~ 5.3 km). This dataset is a blend of satellite and ground observation and has the highest correlation with the real observations (see the supplementary file). The accuracy of CHIRPS data to delineate rainfall characteristics has also extensively been studied (e.g., Ayugi et al. 2019; Kimani et al. 2017; Ngoma et al. 2021). These studies pointed out that CHIRPS dataset reproduces the observed rainfall over East Africa wells. All the aforementioned datasets are analysed for the period of 1980–2018.

The climatological Soil Available Water Holding Capacity (AWHC), also referred as AWC or Root Zone Water Holding capacity was obtained from Oak Ridge National Laboratory Distributed Active Archive Centre (ORNL DAAC) for biochemical dynamics (https://daac.ornl.gov/cgi-bin/dsviewer.pl?ds_id=548). The data has a spatial resolution of $1° \times 1°$. This dataset has extensively been applied (e.g., Dai 2011; Trenberth et al. 2014) in computing sc-PDSI.

Convection is inferred using the daily interpolated National Ocean and Atmospheric Administration (NOAA) OLR data collection (Liebmann and Smith 1996). It is a $2.5° \times 2.5°$ global gridded data set with global coverage. Data running from 1980 to 2018 is used in this study.

Daily datasets from the National Centres for Environmental Prediction–National Centre for Atmospheric Research (Kanamitsu et al. 2002) are utilized to study the circulation anomalies associated with MJO. This dataset comprises meteorological variables (wind, temperature, geo-potential height, humidity on pressure levels, surface variables, and flux variables like precipitation rate). It has a spatial resolution of $2.5° \times 2.5°$ observed 4 times a day at 0000, 0600, 1200 and 1800 UTC, with 17 pressure levels from 1000 to 10 hPa. This study used daily values from January 1, 1980, and December 31, 2018.

2.3 Methodology

2.3.1 Computation and self-calibration of palmer drought severity index

Among the most commonly adopted drought index for assessing the duration and severity of droughts is the PDSI (Aiguo et al. 2004; Wellet al. 2004; Hua et al. 2011; Palmer 1965). The PDSI is determined using an elaborate water balance procedure that integrates past data on temperature, precipitation, AWHC, and possible evapotranspiration. The complete PDSI calculation technique includes various quantitative variables that are assessed depending on the hydrothermal conditions of the study area. As a result, the PDSI's shortcomings in regional hydrological studies are apparent. As a consequence, since it uses a significant number of climate variables as data, this index gives a detailed instrument for assessing global warming impact drought (Dai 2013; Liu et al. 2012). Wells et al. (2004) presented the sc-PDSI as an enhanced form of the "classical" PDSI. For the purposes of clarity in the self-calibrating PDSI calculation technique, we commenced with Palmer (1965) PDSI computation. The symbol without a subscript indicates the initial variable for the PDSI calculation. Using a water balance model, the water deficit, d, can be calculated.

2.3.1.1 Step 1: Computation of water deficiency, d The determination of the PDSI value for a particular month in a particular year begins with the calculation of water balance model elements depending on precipitation, temperature, and AWC. Based on the recorded precipitation and the precipitation under the Climatically Appropriate for Existing Condition (CAFEC), the water deficit, d, may be calculated. The water balance model uses ET (evapotranspiration), R (recharge of the actual world soil moisture), RO (runoff), L (loss of the real world soil moisture), and PE (potential evaporation), PR (potential soil moisture recharge), PRO (potential runoff), and PL (potential soil moisture loss) to calculate d. The PET was

calculated using the Thorthwaite algorithm (Thornthwaite 1948). On the basis of actual precipitation and prospective evapotranspiration, the Double-Layer Soil Model (DLSM) was used to determine the remaining water balance elements.

The DLSM analysis separated the soil layer into two distinct portions (Eq. (1)). As a result, the AWC consisted of two distinct components: the AWC of the surface soil layer (AWC $_s$), which measured approximately 1 inch (or 25.4 mm), and the AWC of the underlying soil layer (AWC$_u$), which measured approximately 9 inches (or 228.6 mm):

$$AWC = AWC_S + AWC_U \tag{1}$$

During the first few days of the month, we assumed that the initial moisture content of the surface soil and the layer underneath is, S_s and S_u respectively (Eq. 2). During the first month, the moisture content of the surface soil equals the AWCS, whereas the moisture content of the soil beneath the surface equals the AWCU. The S_s and S_u values for subsequent months can be calculated using the observed values of soil moisture in the real world for the months that came before them. The difference between the effective soil moisture and the real-world observed soil moisture is the highest potential water retention (PR) that the soil volume can hold (Eq. (2)):

$$PR = AWC - (S_s + S_u) \tag{2}$$

The PRO is the total soil moisture, which is determined using Eq. (3):

$$PRO = S_s + S_u \tag{3}$$

According to DLSM, when rainfall is insufficient to fulfil ET, the soil moisture of the surface soil layer can supplement ET's water inadequacy, while the soil moisture of the subsurface soil layer can partially satisfy ET. In this instance, the PL of the DLSM was calculated using Eqs. 4, 5, 6:

$$PL = PL_s + PL_u \tag{4}$$

$$PL_s = \min(PE, S_s) \tag{5}$$

$$PL_u = (PE - PL_s) \cdot \frac{S_u}{AWC} PL_u \leq S_u \tag{6}$$

The ET, R, RO and L can be computed based on P and PET: given PET $\leq P$, ET$=$PET, $L=0$, $R=0$, RO$=P-$ET$-$PR; given PET$>P$, ET$=P+L$, RO$=0$, $L=L_s+L_u$, $R=\min$ (PE$-P$, PR). Where the elements of the DLSM are derived using (Eqs. 7 and 8).

$$L_s = \min(PE - P, S_s) \tag{7}$$

$$L_u = (PE - P - L_s) \cdot \frac{S_u}{AWC} PL_u \leq S_u \tag{8}$$

On the basis of the previously discussed water balance elements, the remaining water balance elements can be derived by (Eqs. 9, 10, 11, 12):

$$\widehat{ET} = \alpha_i PE \tag{9}$$

$$\hat{R} = \beta_i PR \tag{10}$$

$$\widehat{RO} = \gamma_i PRO \tag{11}$$

$$\hat{L} = \delta_i PL \tag{12}$$

where $\alpha_i = \frac{\overline{ET_i}}{\overline{PE_i}}$; $\beta_i = \frac{\overline{R_i}}{\overline{PR_i}}$; $\gamma_i = \frac{\overline{RO_i}}{\overline{PRO_i}}$; $\delta_i = \frac{\overline{L_i}}{\overline{PL_i}}$ i denotes months of a given year and ranges from 1,2,… to 12. α_i, β_i, γ_i, and δ_i denote coefficients of the water balance components related to ith month.

The letter with a straight line cap signifies the average value for a particular month, and $\widehat{ET}$, $\hat{R}$, $\widehat{RO}$, and $\hat{L}$ denote the ET, recharge of soil moisture, runoff, and loss of soil moisture under CAFEC. Then, we determined the water deficit based on the actual rainfall quantity observed in the real world (Eq. 13) and the rainfall quantity under the CAFEC for a particular month (Eq. 14):

$$d = P - \hat{P} \tag{13}$$

$$\hat{P} = \widehat{ET} + \hat{R} + \widehat{RO} - \hat{L} \tag{14}$$

where d represents the water deficit, P represents actual precipitation, and $\hat{P}$ represents precipitation under the CAFEC.

2.3.1.2 Step 2: Determination of Z values The water inadequacy, d, is employed to quantify the variation between the actual precipitation total for the current month and $\hat{P}$ in inches or millimeters. Nevertheless, the $\hat{P}$ value varies from place to place and month to month. Thus, the same d value may indicate varying humidity situations depending on the place and month, e.g., identical water deficit may indicate different drought intensities in arid and humid regions or during the rainy and dry seasons, correspondingly. In this instance, modification factors, K, were implemented to measure water demand and supply relationships in a particular location as in Eq. (15).

We estimate the water requirements with $\overline{PE} + \overline{RO} + \overline{R}$ and the water supply with $\overline{P} + \overline{L}$. We adjusted the water inadequacy, d, to the water deficit index, Z, to accurately represent the variations in moisture and dryness as in Eq. (16).

$$K = \frac{\text{Water Demand}}{\text{Water Supply}} = \frac{\overline{PE} + \overline{R} + \overline{RO}}{\overline{P} + \overline{L}} \tag{15}$$

$$Z = dK \tag{16}$$

Z index is the departure of actual wetness/dryness from the long-term yearly mean water availability in a specific location for a certain month. In arid climates, water requirement exceeds water supply; thus, drought conditions are more dependent on scarcity or water supply in arid areas compared to other places. Hence, $K > 1$ and K operate as a booster and underscores the importance of water supply, which is not advantageous for PDSI-based drought monitoring over a wider area. Considering drought monitoring in a particular region with distinct water availability and other particular geographic characteristics, K value should be modified periodically. The K factor was further enhanced, as demonstrated by Eq. 17.

$$\overline{D}_i = \frac{\sum_{\text{all years}} |d_i|}{\text{Leghth of Years}} \tag{17}$$

The parameter with a small line above it represents the long-term yearly mean of this parameter for a specific month, i.e., D_i represents the long-term yearly average of the absolute value of the water deficiency, d_i, for a particular month, i.e., K'_i is, therefore, the calibrated K value for a particular location during a particular month. Various $\sum \overline{D}_i K'_i$ were determined through evaluations of different locations within the study location; the mean of these values, 17.67, was used as the base case, while the $\sum \overline{D}_j K'_j$ for a particular region was used as the denominator. Once more, the K value was modified (Eq. 18). The succeeding K value can only be employed for drought monitoring in the regions studied by Palmer; it is not applicable for drought monitoring in other geographic areas. A simplified version of K values for a specific month is shown in Eq. (19).

$$K'_i = 1.5 \log_{10} \left(\frac{\frac{\overline{PE_i} + \overline{RO_i} + \overline{R_i}}{\overline{P_i} + \overline{L_i}}}{\overline{D}_i} \right) \tag{18}$$

$$K_i = \frac{17.67}{\sum_{j=1}^{12} \overline{D}_j K'_j} K'_i \tag{19}$$

where K is the moisture anomaly index.

Without taking into account the patterns of the latest rainfall, the Z index can be applied to provide an indication of the level of dryness or wetness experienced during a given month. You can also use it to approximate the value of the PDSI for a particular month by using Eq. 20, which is as follows:

$$X_i = 0.897 X_{i-1} + \left(\frac{1}{3}\right) Z_i \tag{20}$$

The only distinction between the PDSI and the sc-PDSI is that the empirical constants (K) and the duration factors (0.897 and 1/3) are replaced with values that are automatically created based on the research site's historical climate data This gives the sc-PDSI geographical comparability and calibrates the index's performance at any region (Wang et al. 2015). Sequentially the 98th and 2nd percentile values of the PDSI then finally sc-PDSI is computed as shown in Eq. 21.

$$X_t = \left(1 - \frac{m}{m+b}\right) X_{i-1} + \frac{CZ_t}{m+b} \tag{21}$$

Thus, considering any category of drought, specified as C, the computed index is calibrated as long as m and b can be computed, where m is the line slope and b is the y intercept. Table 1 shows the sc-PDSI values as well as drought categories. The theory of run (Le et al. 2019; Yevjevich 1969) is then applied to the sc-PDSI time series to isolate the most severe droughts and their facets.

2.3.2 Power spectral analysis and wavenumber-frequency filtering

MJO modes characterized by zonal dispersion are investigated using zonal space–time spectral analysis and filtering of OLR data in the wavenumber–frequency dimension. The spectral analysis reveals the power dispersion in the wavenumber-frequency spectrum related to the moving phases. By applying a filter, we can get a rough approximation of the longitude-time pattern typical of various locations in the wavenumber-frequency dimension. Studies (e.g., Wheeler and Kiladis 1999; Roundy and Janiga 2012; Roundy 2012) applied a similar approach to figure out the spectral characteristics of Intra-Seasonal Oscillations' spectral characteristics. To initiate the spectral analysis, the yearly periodicity was determined at every grid point by standardizing a sequence of daily means. This annual loop was eliminated to create a collection of anomalies.

Table 1 PDSI classification (Palmer 1965)

PDSI category	Weather	PDSI category	Weather
> 4.00	Extremely wet	< − 4.00	Extreme drought
3.00–3.99	Very wet	− 3.00 to − 3.99	Severe drought
2.00–2.99	Moderately wet	− 2.00 to − 2.99	Moderate drought
1.00–1.99	Slightly wet	− 1.00 to − 1.99	Mild drought
0.50–0.99	Incipient wet spell	− 0.50 to − 0.99	Incipient drought
0.49	–	− 0.49	Near normal

The anomalies at every latitude were then grouped into sixty globally zonal 97-day temporal pieces that spanned 65 days and intersected one another.

The periodic average, regular and parabolic tendencies were eliminated from each component to exclude pulses with frequencies less than or equal to 1/97 cycles per day. The zonal space–time spectral calculations for every section were computed by decaying the portions into sophisticated wavenumber and frequency aspects for eastward and westward-moving perturbations (Roundy and Janiga 2012) using a discrete Fourier transform in space preceded by one in time, and then calculating the product of this decay and its sophisticated conjugate. Based on the specified spectral structure, the generated power was then averaged across all relevant portions and all appropriate latitudes or latitude permutations. In spectrum analysis, only bands reflecting data from 15° N to 15° S were considered is in Wheeler and Kiladis (1999). The statistical significance of spectral power is determined using the red-noise spectrum and the Student's t test. Presented in Eq. 22 is the precise formulation of the red noise spectra p_{rn}.

$$p_{\text{rn}}(k, w) = \frac{\sigma_z^2(k)}{1 + \alpha_1(k)^2 - 2\alpha_1(k)\cos(2\pi\omega)}, \tag{22}$$

where k is zonal wavenumber, ω is frequency, σ_z^2 is the variance of driving white noise, and 1 is lag-1 autocorrelation coefficient computed from the observed time series whose longitudinal component is transformed into wavenumber space. In Eq. 1, σ_z^2 is chosen so that it is equivalent to the amplitude of the original spectrum when integrated over frequency at each wavenumber.

Transforming the time-domain wavelet transform of OLR anomalies down the long axis yields the space–time wavelet transform Eq. (23). Morlet's wavelet,

$$\varphi(s) = \frac{1}{\sqrt{\pi B}} \exp(i\sigma s) exp\left(-\frac{s^2}{B}\right) \tag{23}$$

is applied, where s represents x or t for the spatial or temporal transforms, respectively, and s represents angular frequency, v or wavenumber, k. The bandwidth parameter B was assigned a value of $4(v/2\pi)^{-3/2}$ for the temporal transform and $1.5(k/2\pi)^{-3/2}$ for the spatial transform.

The above procedure can be summarized step by step as:

1) Longitude–time arrays of OLR anomalies are used to organize the data.
2) To create symmetric filtering, both north and south latitudes are added or subtracted from each other and then divided by two in the following phase (for asymmetric filtering).
3) These several 96-day segments that overlap each other by 48 days are the product of symmetry filtering. After that, the segments' linear temporal trends are removed and they are progressively tapered in time using a sine function called cosine bells (to reduce spectral leakage). As a consequence of the tapering, some wavelet transform may have been removed.
4) Afterwards, the Fourier transform is done throughout the longitude spectrum.
5) The coefficients obtained as a result are converted in time.
6) The spectral power of the resulting complex arrays is obtained by multiplying them by the complex conjugates of the producing complex arrays.
7) The power of each segment is averaged throughout the entire collection of segments to get a mean spectrum.
8) Once the symmetric and antisymmetric spectra have been calculated, they are smoothed 30 times with a 1-2-1 filter to obtain an approximation of the background spectrum for each spectrum.
9) The normalized spectrum is calculated by dividing the original spectrum by the smoothed background.

Longitude-time arrays of anomalous OLR aggregated between 30° N and 30° S are translated in longitude and time (without regular segmentation) to extract MJO features with unique phase speeds from the OLR. The wave-number-frequency field's related factors are decreased to zero, focusing on eastward propagation beyond the required phase speeds band. Using the spatial–temporal inverse Fourier transform, it is possible to acquire filtered (Kiladis et al. 2005; Ventrice et al. 2013).

2.3.3 Variance analysis

The following procedure was used to determine the proportion of variance attributable to the MJO and each of the equatorial wave types. To begin, the original data was subtracted from the 39-year mean and the first three harmonics of the seasonal cycle. Second, each grid point's standard deviation was used to partition the daily anomalies. The wavenumbers and frequencies associated with each wave type were then filtered from the standardized anomalies. Each wave type's share of the total variance is represented by the variance of these filtered values.

2.3.4 Lagged regression composite analysis

To study the MJO-filtered OLR bands' spatial structure and evolution, we used a variety of methods. To begin, the OLR filtered by the MJO was gathered at a starting location (39° E, 1° N). Relying on a reference grid point over Kenya (1° N, 39° E), a time series, henceforth known as the MJO

index, was generated. The MJO index consists of all days where the minimum negative MJO-filtered OLR was less than − 1.5 standard deviations during the active/negative phase and days where the maximum positive MJO-filtered OLR was greater than + 1.5 standard deviations during the suppressed/positive phase during the 1980–2018 time frame. In the remaining time series, we determined the dates of all peaks and minima that were more than two standard deviations apart ($\pm 2\sigma$). To create lagged composites for a given field, the data were averaged over these dates so that the highest amplitude occurred on day zero. Linear regression has previously been used to construct symmetric composites between positive and negative phases (e.g., Klotzbach 2010; Schreck 2021; Ventrice et al. 2013). It was possible to create time-varying composites by merely averaging data points from extremes of the same sign, as in Roundy (2008). Composite anomalies were tested for statistical significance using a bootstrap test similar to Wheeler and Kiladis (1999) method. Null examples were detected in this test utilizing the same months and days as the original composite but from the other 37 years of the period in question.

For example, on January 13, 1981, the maximum filtered value occurred, and every January 13 from 1980 to 2018 and from 1982 to 2018 would be considered null cases. The baseline composite was contrasted against randomly selected null dates from the null cases to create the null composites. These composites were generated 1000 times by repeating this procedure. A two-tailed test indicates that an anomaly at a specified grid point in the original composite was 95% significant if it occurred in 975 of the 1000 null composites. This statistical test is valid since it considers sample size and seasonal fluctuation. The daily datasets are initially filtered using Lanczos (1950) technique to reduce the noise inherent in the data.

2.3.5 Characterisation of drought

Probability Density Function (PDF) plot is used to characterise droughts in this study. Previous studies by Kalisa et al. (2020) and Ongoma et al. (2018) successfully applied PDF to examine the drought and precipitation characteristics over East Africa (EA), respectively. The initial step of plotting PDF in this study begins with the determination of the frequencies. In this study, the frequencies are expressed as counts of individual droughts events that falls within a given drought category as described in Table 1. The drought frequencey, F, determined as in Eq. 24.

Equation 24 Determination of drought frequency

$$F_j = \frac{\sum_{i=1}^{m} M}{N} \times 100\%$$ (24)

In Eq. 24, N is the length of the time series (from 1980 to 2018 = 39 years) and m is the number of drought events in a given Palmer category/class; M is the drought category. To compute the cumulative frequency: the first category has the cumulative probability of itself. The next category is the sum of the previous category and itself and all were expressed in percentage as obtained from Eq. 24. The cumulative frequency tells you the probability of drought being below a given category. The next step is to compute the probability of exceedance. The probability of exceedance signifies the probability of drought being above the given category. It is simply the maximum probability minus the probability of the drought being below the category. To compute it: subtract the cumulative probability of a given category from the maximum probability and is similarly expressed as a percentage.

3 Results and discussions

### 3.1 Historical dry events and their characteristics

The extreme events are identified using the sc-PDSI as discussed in Sect. 2.3.1. The most severe dry spell was experienced between March 1983 to March 1988 lasting 61 months followed by the Oct 1998 to Oct 2001 dry spell which lasted for 37 months. The severe droughts peaks captured by the sc-PDSI runs were February 1981, August 1984, April 1992, June 1994, February 1997, June 2001, July 2011, June 2014. The period in which the dry events were experienced during the study period is shown in Table 2. These results are in concurrence with Balint et al. (2013) which identified 1983–1984, 1992–1993, 1999–2000, and 2009–2011 as some of the drought years though using different approaches to study drought. It is evident that there has been a decline in the severity of drought over the last decade. However, it is not clear what might be contributing to this shift of events given that recent studies (Dai 2013; Ongoma et al. 2018) have presented results indicating an increase in the frequencies and severity of the drought events over the larger East African domain. The relationship between the sc-PDSI time series and MJO is later examined in Sect. 3.6.

The annual distribution of the sc-PDSI values based on Table 1 from 1980 to 2018 is presented in Fig. 2. Mild droughts and extreme droughts account for the highest percentage of the drought categories with 15.38 and 12.82%, respectively. While moderate and severe droughts accounted for 5.13 and 2.56%, respectively. The probability of exceeding the extreme drought category is very low at 0% while the probability of exceedance of the mild, moderate and severe drought categories are 20.5, 15.4 and 12.8%, respectively. Generally, more wet periods were observed compared to the dry periods as depicted

Table 2 The duration, severity, intensity and inter-arrival of occurrence of some of the major historical (1980–2018) dry events (scPDSI ≤ − 1) in Isiolo County, Kenya

Period of occurrence	Duration (months)	Peak	Severity	Intensity	Inter-arrival (months)
Jan 1980–Feb 1981	12	Feb 1981	33.294	2.774500	20
Nov 1981–Mar 1982	5	Mar 1982	10.759	2.151800	16
Mar 1983–Mar 1988	61	Jun 1984	126.412	2.072328	97
Apr 1991–Dec 1992	21	Apr 1992	45.837	2.182714	23
Mar 1993–Sep 1994	19	Jun 1994	37.510	1.974211	35
Feb 1996–Mar 1997	14	Feb 1997	29.174	2.083857	32
Oct 1998–Oct 2001	37	Jun 2001	117.092	3.164649	53
Mar 2003	1	Mar 2003	1.402	1.402000	25
Apr 2005–Feb 2006	11	Feb 2006	17.582	1.598364	33
Jan 2008	1	Jan 2008	1.007	1.007000	4
May 2008–Jul 2009	15	Jun 2008	17.895	1.193000	29
Oct 2010–Aug 2012	23	Apr 2012	38.609	1.678652	36
Oct 2013–Feb 2015	17	Jun 2014	24.718	1.454000	36
Oct 2016	1	Oct 2016	1.081	1.081000	7
May 2017–Jul 2017	3	Jun 2017	3.511	1.170333	20

Fig. 2 Probability Density Function (PDF) of the annual drought categories histograms represents the frequency (%), while the red and green lines represent the cumulative frequencies (%) and the probability of exceedance (%)
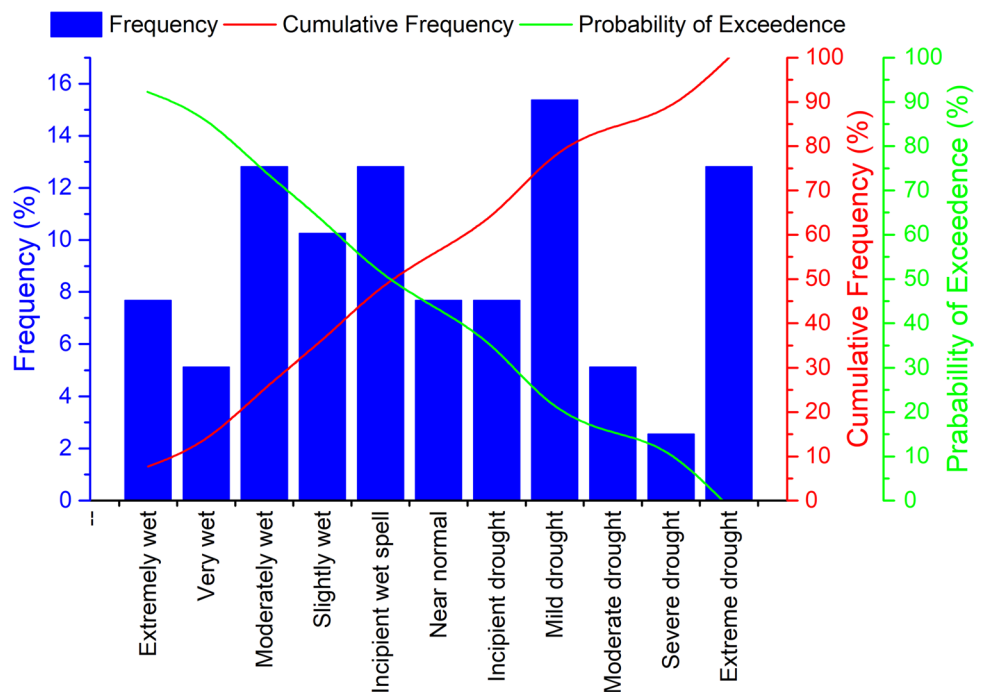
by the high frequencies. The frequent occurrence of these extreme weather events can be alluded to be driven by climate change and other anthropogenic causes (IPCC AR6 2022). This trend of continuous wet and hot scenario is projected to remain the same in the future (Ochieng et al. 2022). Therefore, there is a need to have resilience mechanisms adopted to minimize these uncertain climate hazards which have a high potential of causing both environmental and socio-economic destructions.

3.2 Time evolution and process analysis for Kenya's 2013–2015 drought

The failure of the 2013 short rains resulted in a devastating drought that lasted through the 2014 long rains and short rains long rains. A long-term lack of precipitation directly caused the 2014–2015 drought. Figure 3 illustrates the climatological distribution of the seasonal rainfall over Kenya. Higher rainfall intensity is observed during the MAM and

Fig. 3 Distribution of mean seasonal rainfall over Kenya (mm/month) **a** MAM, **b** JJA, **c** OND, **d** DJF
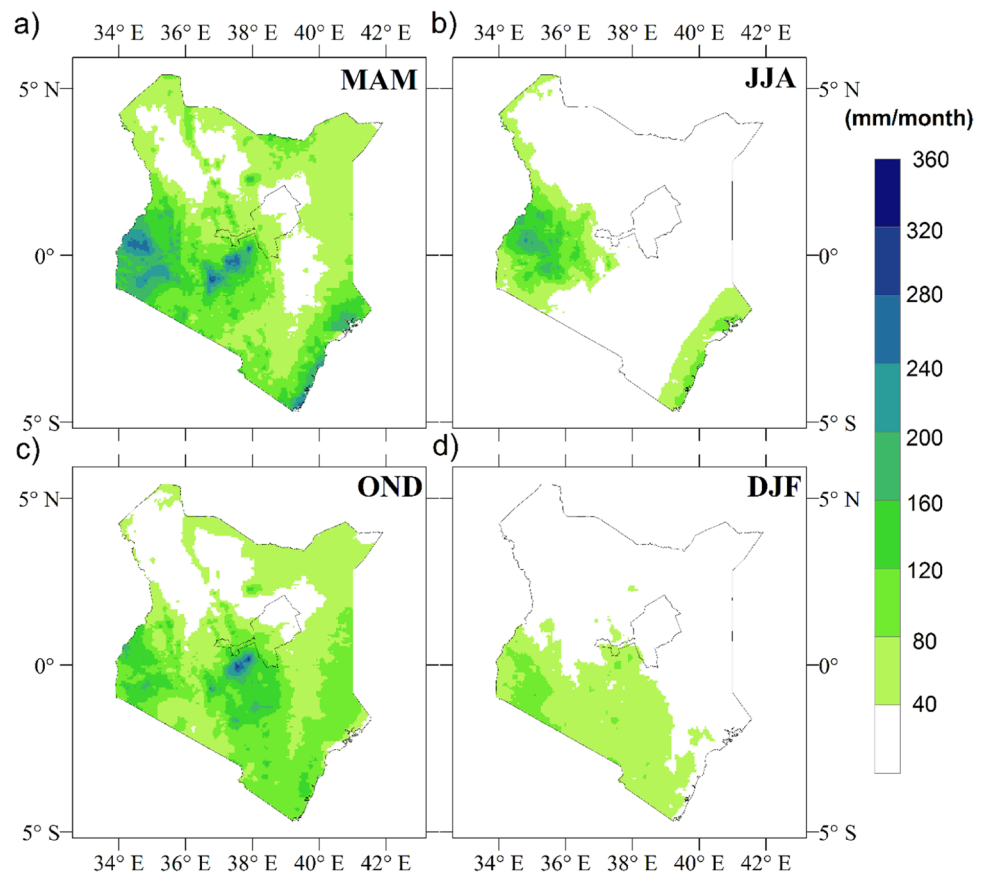

OND seasons when Kenya receives long and short rains. During these seasons, the western zones and the central highlands record higher rainfall amounts than other locations. Rainfall is suppressed during the DJF (Fig. 2d), with the climatologically rainfall received being less than 40.mm/month. The seasonality of rainfall is influenced by the ITCZ with the two latter-mentioned rainfall maxima being experienced when the ITCZ is over Kenya during MAM and OND (Ongoma et al. 2015). The rainfall displays great spatial heterogeneity due to the varied geography, including steep mountains and valleys, as well as huge water basins like Lake Victoria along the Kenya-Uganda-Tanzania border and the adjacent Indian Ocean (Hession and Moore 2011). The fluctuations in global Sea Surface Temperatures (SSTs) have the most significant effect on the inter-annual precipitation patterns. ENSO (Indeje et al. 2000b) and the Indian Ocean Dipole (IOD) (Owiti et al. 2008; Owiti and Ogalo 2014) are some of the outcomes of SST anomalies in the Pacific and Indian Oceans. The complexity of droughts' spatial–temporal characteristics is determined by atmospheric teleconnection patterns and Intra-Seasonal Oscillations such as MJO (Kalisa et al. 2020; Le et al. 2019; Vicente-Serrano 2005). The linkages between drought conditions and MJO can be observed at a seasonal scale (Dai 2011; Trenberth et al. 2014).

Figure 4 illustrates the spatial distribution of the percentage departure of the seasonal rainfall determined based on Yang and Wu (2010) for 2013/2014. The failure of the short rains of 2013 forms the drought genesis. It is evident that during the latter season, the central and eastern locations of the country are adversely affected by rainfall deficiency, with below more than 40% rainfall being observed. This was followed by poor rainfall performance during MAM 2014 season (Fig. 4b); it is inherent that most western parts of the country received less rainfall than the long-term mean values, with these regions recording 50% fewer rainfall amounts. Even though 2014 JJA (Fig. 4c) appears to have positive percentage departures, the spatial distribution is poor. Since drought is aggravated by the persistence of water deficit caused by an imbalance in the water system, failure of the subsequent OND 2014 (Fig. 4d) rains shown by the negative percentage departures over the central, eastern and north-eastern zones led to a humanitarian crisis of 2015.

3.3 Seasonal dependancy of MJO

To identify ISO-related variability in raw OLR, we employ wavenumber-frequency spectrum analysis. Approaches comparable to Wheeler and Kiladis (1999) are used in this study. OLR outgoing long-wave radiation (OLR) data show power

Fig. 4 Distribution of rainfall percentage departures from normal over Kenya in 2013/2014 **a** 2013 OND, **b** MAM 2014, **c** JJA 2014 and **d** OND 2014
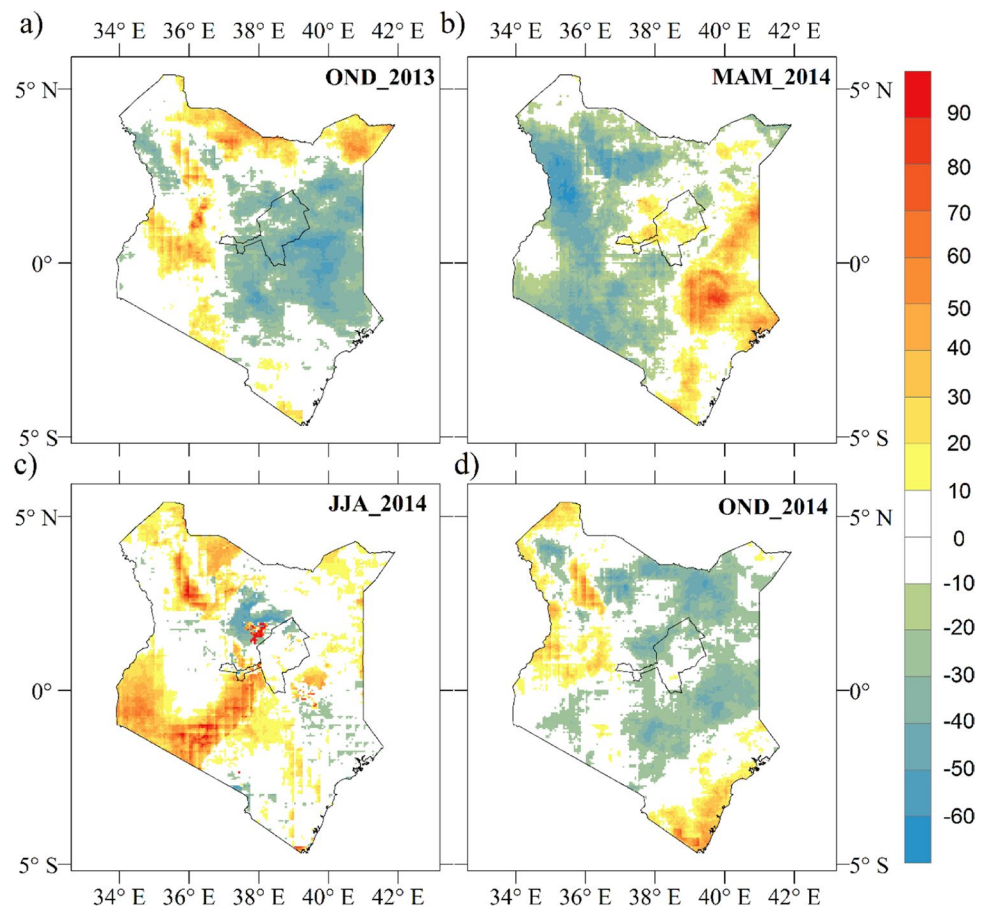
spectrum maxima that are equivalent to Kelvin waves, equatorial Rossby waves, mixed Rossby gravity (MRG) waves, and inertia gravity (IG) waves' dispersion features (Roundy 2018; Roundy et al. 2009; Roundy and Frank 2004; Wheeler and Kiladis 1999) For deep tropical convective activity, the spectral distribution of the daily raw OLR can be utilized as a proxy (Fig. 5). As a further inspection of the figures shows, a constant frequency of around 0.25 Cpd and zonal wavenumbers of zero to nine symmetrically around longitude 0°, which is not along any of the theoretical equatorially limited wave dispersion curves, is shown to reflect the MJO. Findings from these studies are consistent with those of Roundy et al. (2009) and Kiladis et al. (2005). There is a low frequency of MJO occurring in these eastward propagating atmospheric disturbances with a periodic cycle of 20–100 days, which is analogous to the results found by Okello et al. (2021) for the convectively coupled equatorial Kelvin waves (CCEKWs) with a periodic cycle of 2.5–18 days. To illustrate the seasonal differences in MJO activity, the intensity of the red background colour is used. While the OND and DJF seasons have the least amount of activity, the seasonal distribution of the eastward propagating ISOs suggests that MJO activities are more prominent during the MAM season. It has been found that MJO activity

accounts for 20% of intraseasonal rainfall variability during the MAM and OND seasons over equatorial East Africa's western areas, which include Kenya and Uganda. Berhane and Zaitchik (2014) found out that the regional and magnitude of MJO influence over East Africa varies from month to month and thus is seasonal as in Figs. 4 and 5. They concluded that the regions that MJO significantly impacts are located within the proximity of the meridional arm of the ITCZ. Enhanced rainfall is experienced when the MJO convective centre is between 20° E and 140° E and dry anomalies prevail when the MJO is located in the region from 140° E to 10° W.

3.4 Geographic distribution of MJO-filtered OLR variance

Figure 6 depicts the seasonal distribution of the fraction of daily total OLR variance falling inside the MJO filter band in Kenya over the four main seasons from 1980 to 2018 (as averaged). These maps, which were generated following the procedures outlined in Sect. 2.3.3, show where MJO activity can be found. During the JJA and OND seasons Fig. 6b, c, respectively, the most significant OLR power is observed over the Arabian Gulf, India, and the Bay of
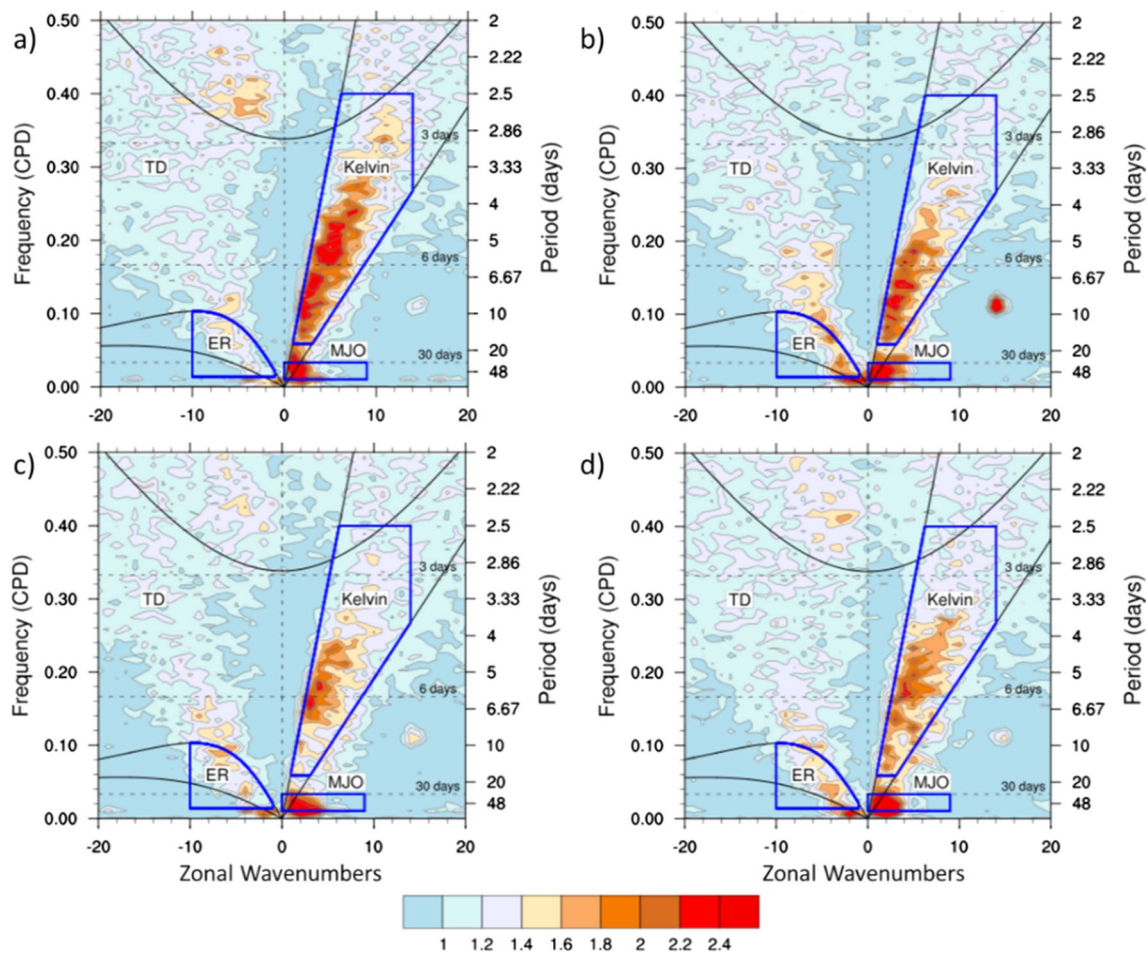
Fig. 5 Wavenumber–frequency power spectrum **a** MAM, **b** JJA, **c** OND, **d** DJF for15° S to 15° N, omitting the equator, divided by a red background. The base-10 logarithm of the power has been plot-ted. Filter bands used in this study are indicated by the cyan boxes. Black lines denote shallow-water dispersion curves for MRG, Kelvin, ER, and inertio-gravity waves with equivalent depths of 8 and 90 m

Bengal. In contrast, the peak values shift eastward during the monsoon season (MAM) as in Fig. 6a, with the western equatorial Pacific region being the focal point. During DJF, the MJO's epicentre is dispersed, with the highest OLR values reported over the Australian continent. MJO's OLR signal (Fig. 6a–d) is cantered in the Indian Ocean and the northern coast of the Australia subcontinent; this is coherent with previous findings (Klotzbach 2014; Masunaga 2007; Roundy 2014; Roundy and Frank 2004; Wilson et al. 2013).

For much of DJF, tropical intra-seasonal convection tends to move east; but, during JJA, it tends to go northeast (Schreck et al. 2013). The boreal summer intra-seasonal oscillation is another name for this phenomenon (BSISO: Kikuchi et al. 2012). The BSISO controls the monsoon activity, which is where the OLR signals are still focused in the Indian Ocean. Tropical cyclone activity in the eastern North Pacific and the Gulf of Mexico is influenced by a secondary signal that appears over the eastern North Pacific

(Aiyyer and Molinari 2008; Kossin et al. 2010; Schreck et al. 2013).

3.5 MJO dispersion in equatorial waves during dry and wet weather events

Individual events' time–longitude sections show the westward group velocity of the MJO without the requirement for compositing. Using the (Wheeler and Kiladis 1999) and (Kiladis et al. 2005) techniques, OLR anomalies of the 20–100-day filtered and MJO-filtered OLR anomalies are shown in Fig. 7. There are three strongest occurrences in each column, and they are located in three different continents and oceans: the Indian Ocean (5° N–5° S, 60°–100° E), the Maritime Continent (5° N–5° S, 100°–120° E), (5° N–5° S, 30°–120° W), eastern Pacific and the western Pacific (15° N–15° S, 140° E–180°). Waves in several of these sequences are grouped in westward-migrating packages. Beginning with the first wave at or east of the Maritime Continent, between 120° E and the dateline,
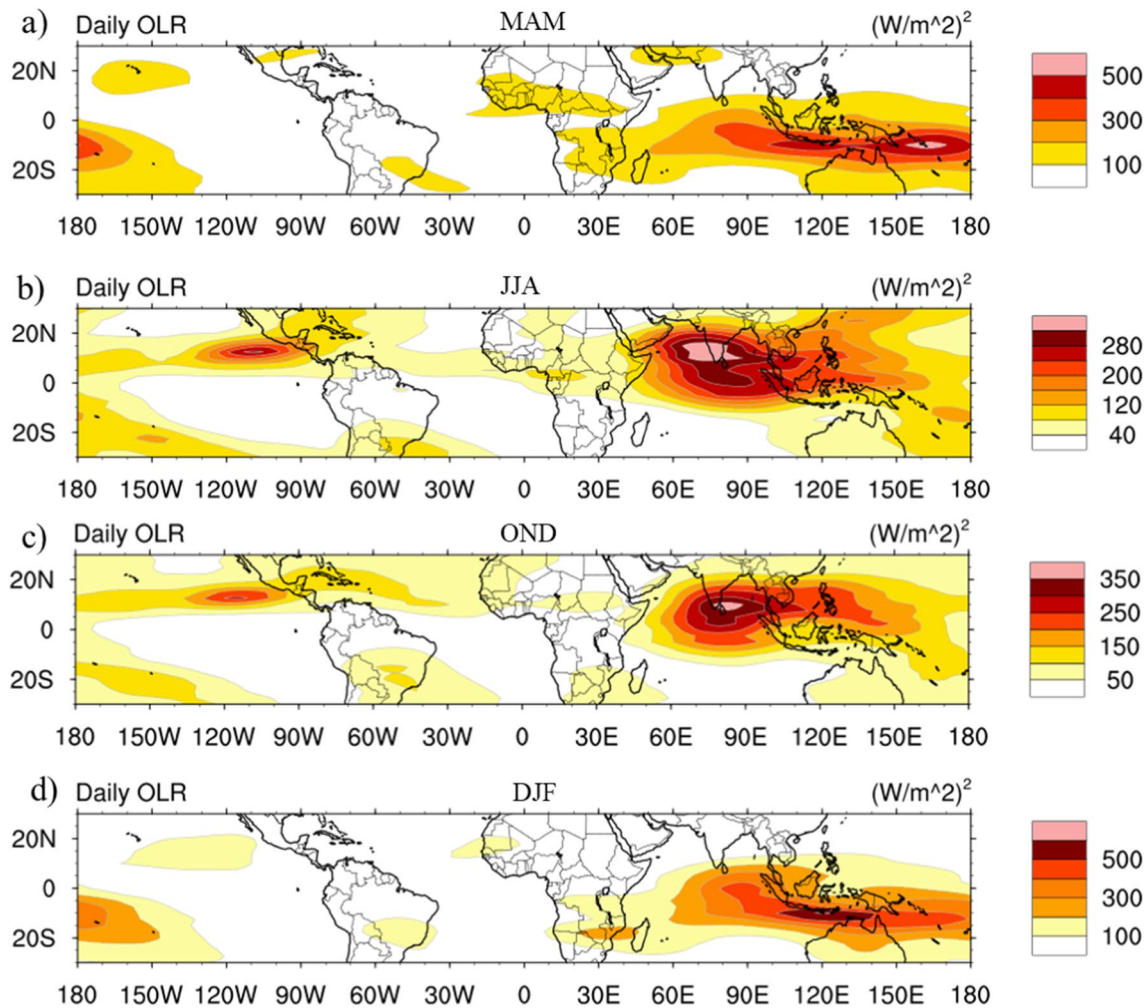
Fig. 6 Geographical distribution of Seasonal MJO band of daily filtered OLR (shading;Wm^{-2})

subsequent waves move westward. Mid-latitude Rossby waves and dispersive equatorially trapped waves like the mixed Rossby–inertial and inertial-gravity modes (Figs. 12, 16, and 20) exhibit similar eastward dispersion. The most conspicuous difference in the features observed in Fig. 6a, b is the Rossby wave signatures over the Atlantic and the Indian Ocean basin is more pronounced during the dry year compared to the wet year. While the MJO and Kelvin waves propagates eastwards the dominant Rossby waves propagates westwards. Figure 6 further suggests that Kelvin waves play a more significant role in rainfall variability compared to MJO during both dry and wet year.

3.6 Physical mechanisms associated with MJO and associated atmospheric circulation anomalies

By applying composites, Berhane and Zaitchik (2014) confirm that there is a relationship between precipitation and MJO indices and that the association is widespread in November–December, March, and May, covering large portions of Equatorial East Africa. The relationship is weaker in October and April. Therefore, this study examined the influence of MJO on convective activities during the rainy MAM season and compared it with the dry DJF season.
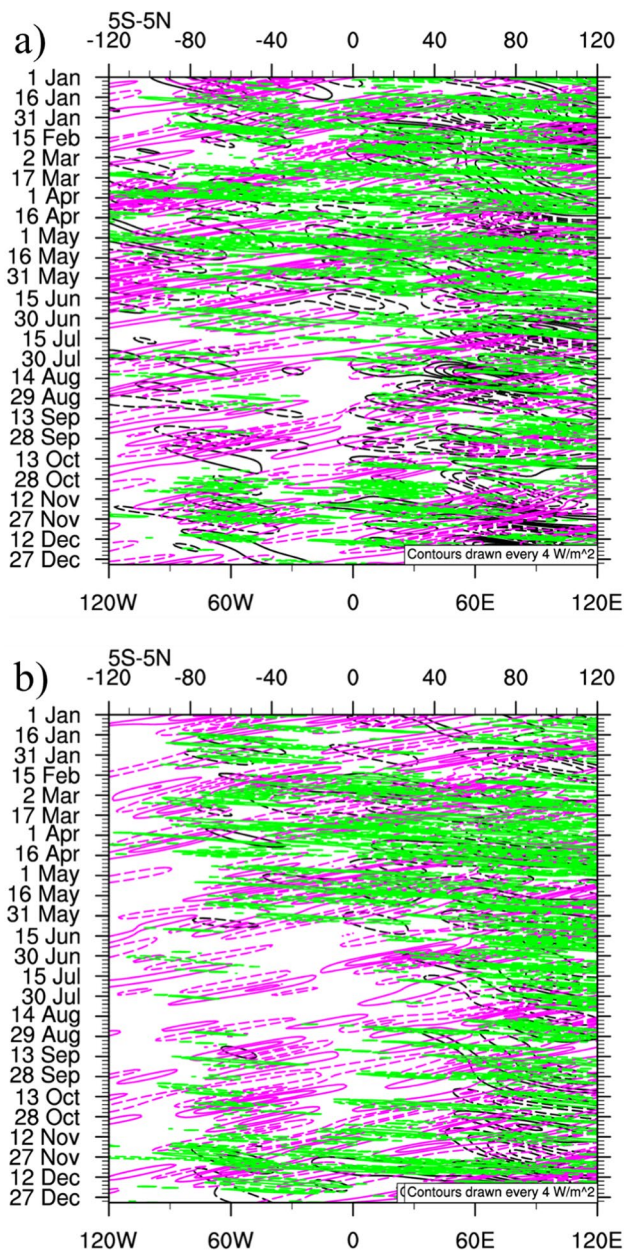
Fig. 7 Time-Longitude section of equatorial waves averaged from 5° N to 5° S during **a** Dry year 2014 and **b** Wet year 2018. The black contours are regions with 95% significant MJO activities, Magenta-Equatorial Rossby and green-Kelvin waves, with the contours are drawn at an interval of 4Wm⁻². The negative contours are dashed while the positive contours are continuous

Fig. 8 a Lag-0 regression patterns as compared with the mean of MJO band filtered OLR anomalies (shading;Wm⁻²), 850hpa wind vectors referenced at point (39° E, 1° N-Green asterisk) for winds ≤ 1 m⁻²s. The contours of 850 hpa geopotential height anomalies (m) are plotted every 1 m with the contours beginning from − 10 to 10 m. The zero contour is omitted. **b** and **c** represent the composite means of the positive and negative events, respectively

850hpa wind anomalies and regressed OLR (shading) and geopotential height (contours) during the lead time of 0 days during MAM are shown in Fig. 8. There are wind vectors when the difference between the values of u/v exceeds the 95 per cent confidence level. It appears that deep convection or enhanced convection is taking place over Kenya's designated base point (39° E, 1° N). The negative 850 hpa geopotential anomalies in the southern Indian Ocean depicts a low-pressure system over the Mascarene region and the Mozambique Channel; this condition is favourable for the meridional movements of the ITCZ due to the resultant east–west pressure gradient created. The latter also leads to moisture flux from the Atlantic Ocean and the moist Congo Air Mass (CAM), enhancing rainfall over Kenya. The difference in OLR power for positive and negative MJO phases are clearly shown in Fig. 8a, b. Negative/positive OLR anomalies are observed during negative and positive events, respectively. A westerly flow may be visible across the western Congo. In the eastern Congo, westerlies are also likely to form. According to positive 850 hPa velocity potential anomalies, 850 hPa flow convergence occurs in the eastern Congo Mountains and the mountains east of the Lake Victoria basin. During DJF (not shown), similar patterns are observed except for negative 850 hPa geopotential anomalies observed during mean adverse events.

Velocity potential was used as a signature for lower (850 hPa) and upper (200 hPa) tropospheric convergence and divergence motions. At upper levels, divergence is usually associated with updrafts from towering cumulus clouds within the proximity of the tropopause as a result of condensational heating. During MAM, positive velocity potential anomalies are observed over east Africa at lag-5 days with easterly lower tropospheric (850 hPa) winds (see Fig. 9c), at lag + 5 days and lag + 10 days positive velocity potential anomalies are observed to have shifted eastwards to the tropical central Indian ocean and
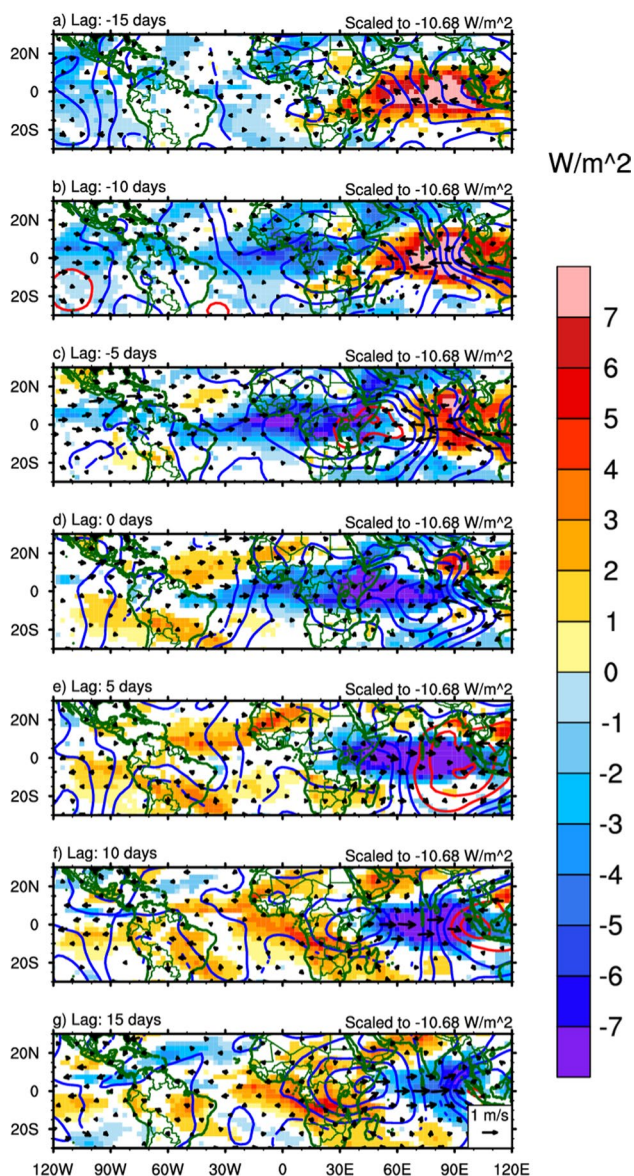
Fig. 9 Lagged regressed MJO filtered OLR anomalies (shading;Wm^{-2}), patterns of mean fields of 850hpa winds vectors referenced at point (39° E, 1 °N), and 850 hpa velocity potential (m^2s^{-1}) contours during MAM drawn from − 10 to 10
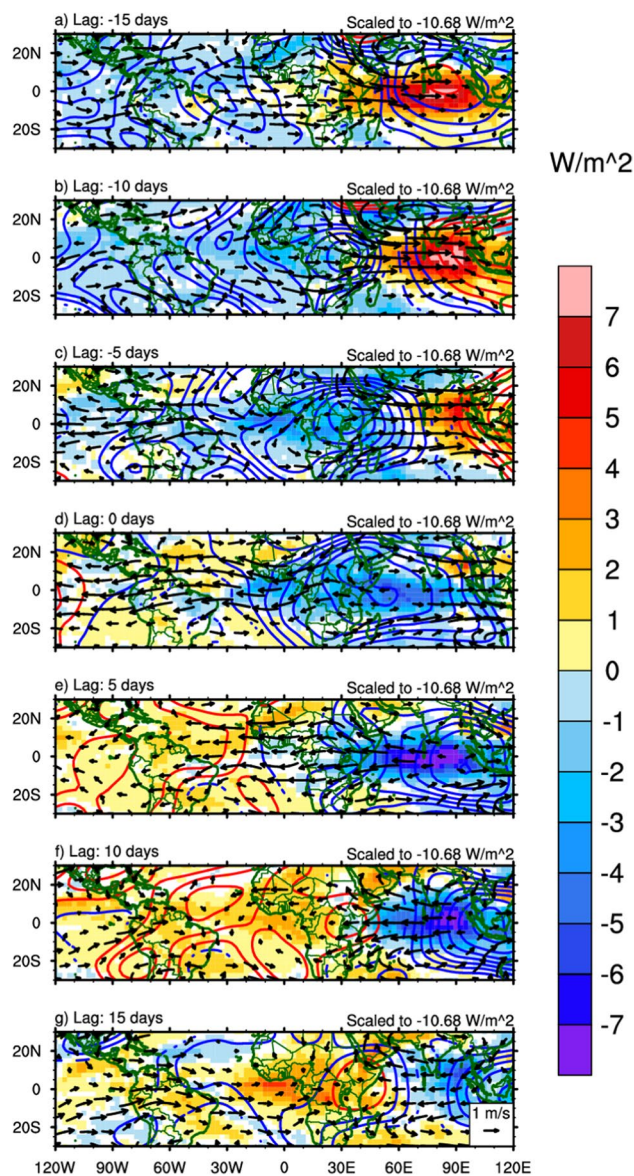

Fig. 10 Lagged regressed Lancoz filtered MJO-OLR anomalies (shading;Wm^{-2}), patterns of mean fields of 200hpa winds vectors referenced at point (39° E, 1° N), and 200hpa velocity potential (m^{2}s^{-1}) contours during MAM drawn from − 10 to 10

the eastern Indian Ocean, respectively. These regions are characterized by low-level convergence. Comparatively, at 200 hPa during the MAM season, upper-level divergence is observed over the central pacific region at lag0 days (Fig. 10d). However, the zones of upper tropospheric divergence are spread over the South American continent, Atlantic at lag + 5 days (Fig. 10e); this is elongated to the entirety of the African continent at lag + 10 days (Fig. 10f). The upper-level winds depict a clear Matsuno-Gill type wave signature with easterly flows on the convectively active zones' western sections and westerly flows on the eastern sections.

Compared with the MAM season, during the DJF season at lag-5 days (Fig. 11c), positive velocity potential anomalies (convergence) are observed over the Gulf of Mexico and East Africa region. Similar observations are also made at lag0 days (Fig. 11d) over the central tropical Indian Ocean during DJF instead of MAM season. The 200 hPa velocity potential at lag + 15 days (Fig. 12g) during DJF shows a different pattern than MAM (Fig. 11g).

All over the Atlantic and African continents, there are areas of convergence at the higher level. Omeny et al. (2008) study statistical relationships between the MJO and Kenyan rainfall from an operational approach. According to the
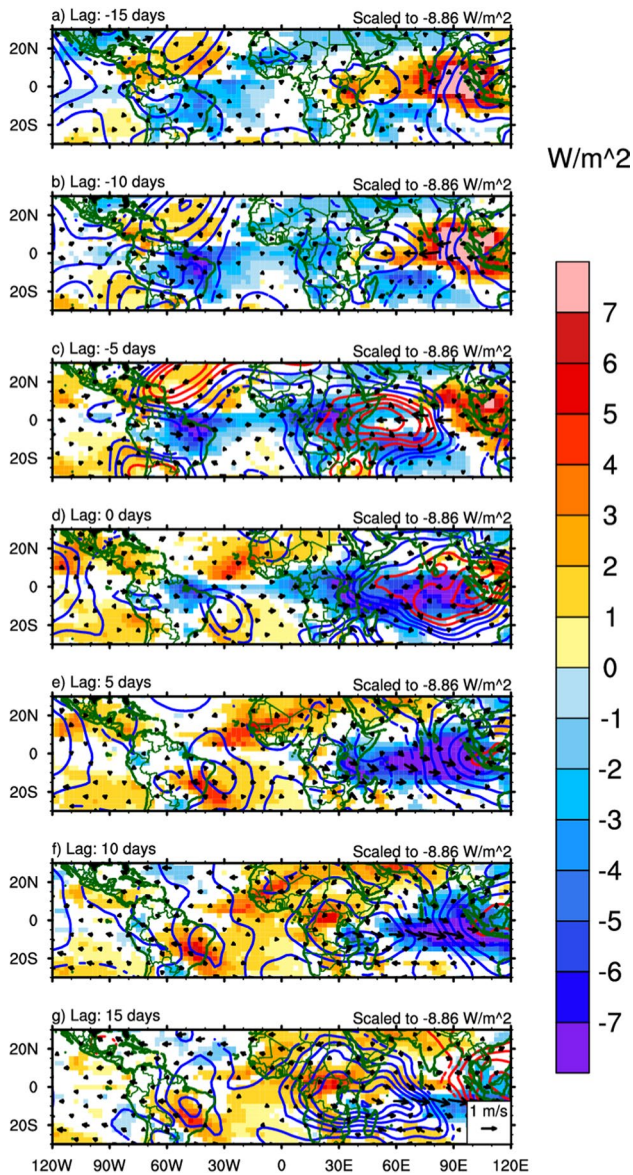
Fig. 11 Lagged regressed MJO filtered OLR anomalies (shading;Wm^{-2}), patterns of mean fields of 850hpa winds vectors referenced at point (39° E, 1° N), and 850hpa velocity potential $(m^2 s^{-1})$ contours during DJF drawn from − 10 to 10
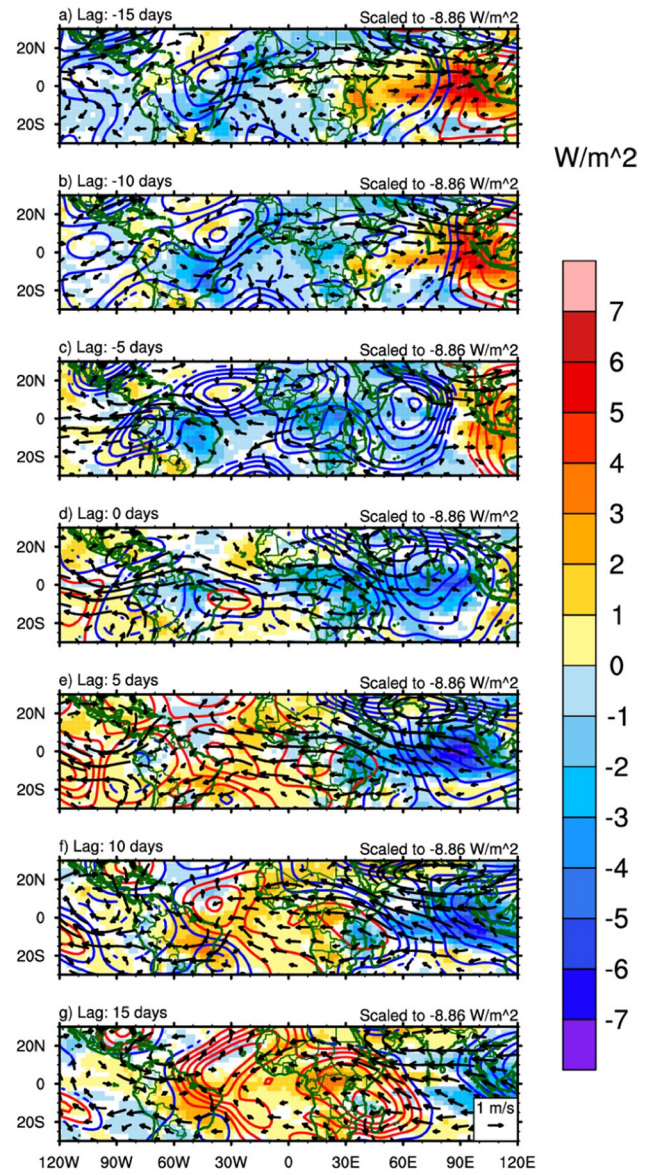
Fig. 12 Lagged regressed Lancoz filtered MJO-OLR anomalies (shading;Wm^{-2}), patterns of mean fields of 200hpa winds vectors referenced at point (39° E, 1° N), and 200hpa velocity potential $(m^2 s^{-1})$ contours during DJF drawn from − 10 to 10

researchers, a strong association between highland rainfall and the MJO occurs when the MJO centre of convection is located in the Indian Ocean. When the MJO advances into the Western Pacific, rainfall in western Kenya decreases. For both short and long rains, the results are the same. For long-range forecasts of 10 days or more, they advocate combining MJO information with other diagnostics to explain a larger portion of the variability in the weather. Omeny et al. (2008) found no significant links between MJO and rainfall in eastern Kenya. Several possible processes of MJO influence are supported by the above-mentioned high precipitation, OLR, and low-level wind anomalies. For example,

increased moisture transport to the region, stronger low-level convergence, and diminished stability in the lower troposphere could increase EA precipitation.

MJO over the tropical Atlantic and Indian Oceans has a vertical wind structure with upper-tropospheric winds (200 hPa) in opposition to lower tropospheric winds (850 hPa) (recall Figs. 9d and 10d). As a result, the vertical wind shear patterns over Kenya and the greater East African region are predicted to be affected by the MJO. Figures 13, 14 show the lagged regression patterns of the MAM and DJF vertical wind shear pattern over the tropical East Pacific, sections of the South American continent, tropical Atlantic,
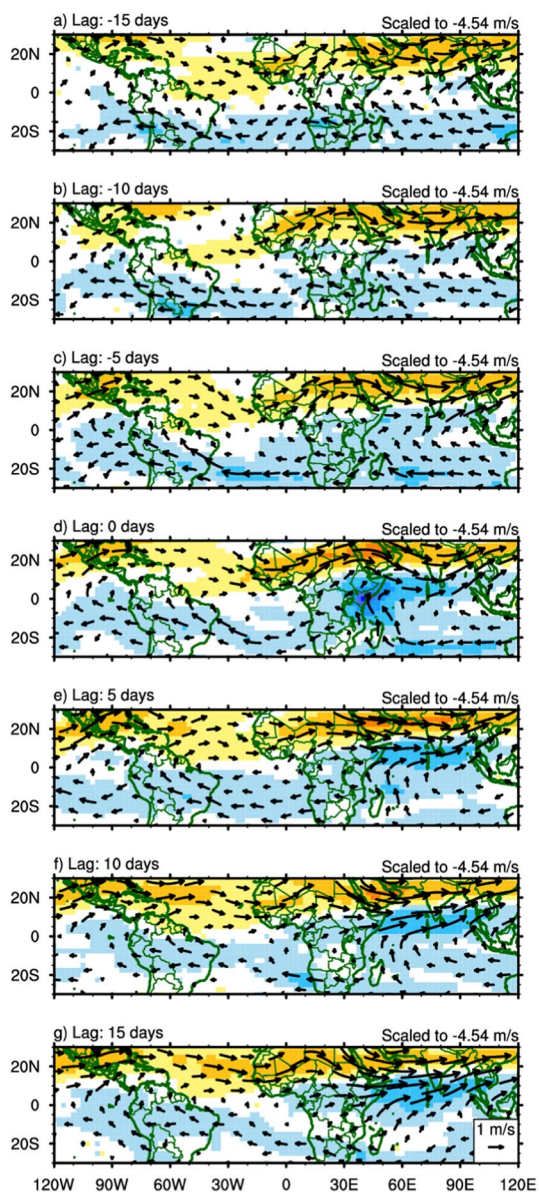
Fig. 13 Lagged regression patterns of the mean field of 850-200hpa wind shear vectors (ms^{-1}) and wind shear vector magnitudes anomalies (shading; ms^{-1}) during MAM
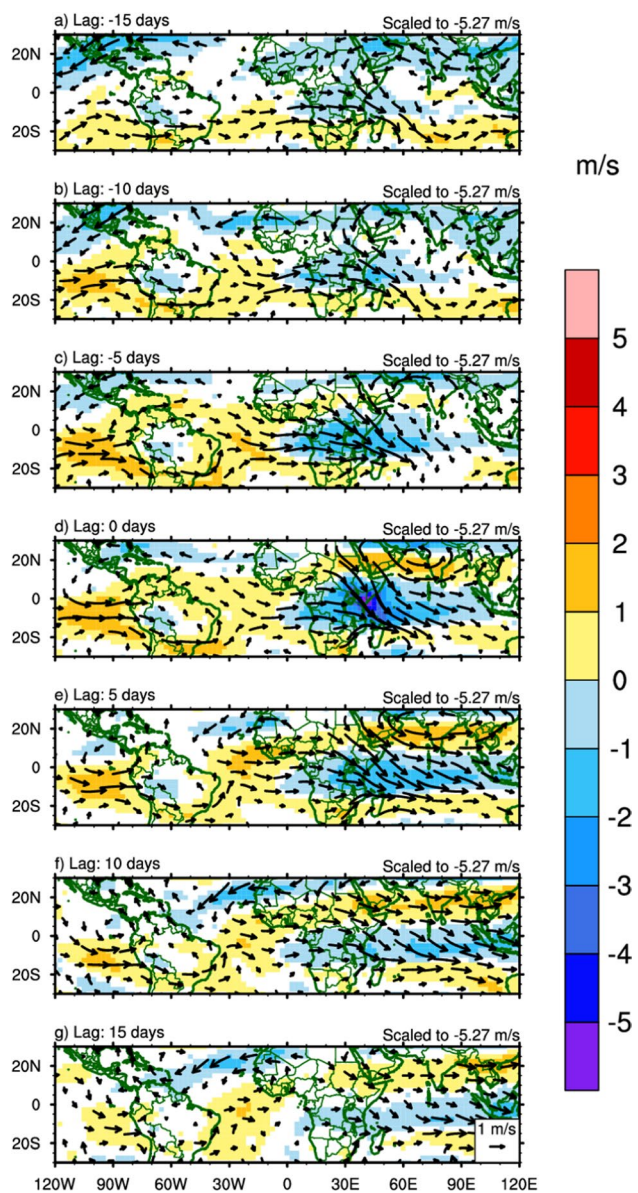

Fig. 14 Lagged regression patterns of the mean field of 850-200hpa wind shear vectors (ms^{-1}) and wind shear vector magnitudes anomalies (shading; ms^{-1}) during DJF

Africa, and the Indian Ocean. This variation in shear direction represents an angle between 850 and 200 hPa. This picture illustrates that the tropical Atlantic is characterized by two different background vertical wind shear states, which agrees with Aiyyer and Thorncroft (2011). Subtropical westerly jets in the western tropical Atlantic are responsible for westerly vertical wind shear, while tropical easterly jets are responsible for the easterly vertical wind shear in the eastern tropical Atlantic.

At positive lags during MAM season, easterly shear vector anomalies occur within and to the west of the active phase of the composited MJO over the west tropical

(Fig. 13d–g), while the westerly wind shear vector anomalies appear to the east of tropical East Africa during the negative lags (Fig. 13a–c). The westerly shear vector anomalies over the tropical Indian Ocean migrate eastward with time as the MJO transitions between the leading convectively suppressed and convectively active phases (Fig. 13a–c). Figure 13f, g depict the development of an anomalous anticyclonic shear signature within the convectively active phase of the MJO at lags of 10 and 15 days, respectively. This anomalous anticyclonic shear signature highlights the atmospheric response to adiabatic heating associated with deep convection (e.g., Dias and Pauluis 2009; Ferguson

et al. 2009; Ventrice et al. 2013). In terms of wind structure, this anomalous anticyclonic signature is similar to the wind structure of the MJO across the Atlantic and parts of South America at lag 5 (Fig. 13c).

During the MAM season, easterly shear vector anomalies occur inside and to the west of the active phase of the composited MJO over the tropics (Fig.13d–g), while westerly wind shear vector anomalies occur east of tropical East Africa during the negative lags (Fig.13e–h) (Fig. 13a–c). Westerly shear vector anomalies move eastward over the tropical Indian Ocean with time, from MJO's leading convectively inhibited phase to its active convective phase. Figures 11f, g show the atmospheric response to adiabatic heating associated with deep convection at lags of 10 and 15 days, respectively, in MJO convectively active phase (e.g., Dias and Pauluis 2009; Ferguson et al. 2009; Ventrice et al. 2013). Wind patterns over the Atlantic and South America at lag-5 of the MJO are similar to this aberrant anticyclonic characteristic (Fig. 13c).

At lag0 during MAM (Fig. 13d) and DJF (Fig. 14d), the anomalous shear signature directions are predominantly westerly to the west and easterly to the east of the active convective MJO zone (see Figs. 9, 10, 11, 12), is coherent with the Gill–Matsuno-type model response to deep convection (Gill 1980). The notable difference between the wind shear patterns is that during DJF, the shear vectors are generally inclined to NW–SE orientation over the Indian Ocean basin (Fig. 14e–g), while during MAM the orientation is mainly Easterly (Fig. 13e–g). Over the east pacific region during MAM westerly shear vectors were observed from lag 10–15 days (Fig. 13f, g), during DJF 10–15 days after the passage of convective MJO band (Fig. 14f, g), over the eastern Pacific and South American regions are characterized by cyclonic flows. Anticyclone shear signatures are also observed over the southern Indian Ocean 5–15 days after

the passage of the MJO during MAM (Fig. 13e–g). For this paper, it is unlikely that tropical cyclone intensity and structure will significantly impact our understanding of climate change. When cyclones are prevalent in the southwest Indian Ocean, Ethiopia can experience drought conditions. Shanko and Camberlin (1998) demonstrated this previously.

EEA convection occurs when the MJO low-pressure centre is in the western Indian Ocean due to westerly wind intrusions are drawn into the region (Pohl and Camberlin 2006). In the mountains and coastal plains of the EEA, the MJO and rainfall have a special relationship, according to the authors of the paper. The MJO has a substantial link with coastal rainfall anomalies, but this correlation is out of phase with respect to the highlands, with enhanced coastal rainfall occurring before the MJO arrives in the EEA region. As a result of MJO-associated low pressure in the Atlantic sector, more significant easterly trade winds may bring moist air from the Indian Ocean into the coastal EEA, resulting in increased coastal rainfall. According to Pohl and Camberlin (2006a), this anomaly in coastal rainfall is strati form in type and does not reflect strong OLR anomalies associated with deep convection.

The temporal all-year relationship of sc-PDSI, MJO index and rainfall extracted at base point 39° E, 1° N is presented in Fig. 15. The most intriguing observation is that the MJO and rainfall are either in phase or out of phase. It is observed that MJO is in phase mainly during El-Nino years, with 1997 being the most notable. A weak correlation exists between MJO and rainfall/sc-PDSI of 0.27 and − 0.29, respectively. Previous studies have found that the influence of MJO over the East coast of Africa is not direct but indirect through the modulation of atmospheric circulation anomalies. For instance, Okello et al. (2021) found a Walker circulation-type air-sea interaction pattern associated with the active phase of convectively coupled Kelvin waves (CCKWs).

Fig. 15 Time series plot of yearly averaged (1980–2018) values of sc-PDSI (black solid line), OLR-MJO filtered band (red solid line) and the annual total rainfall (mm/year)
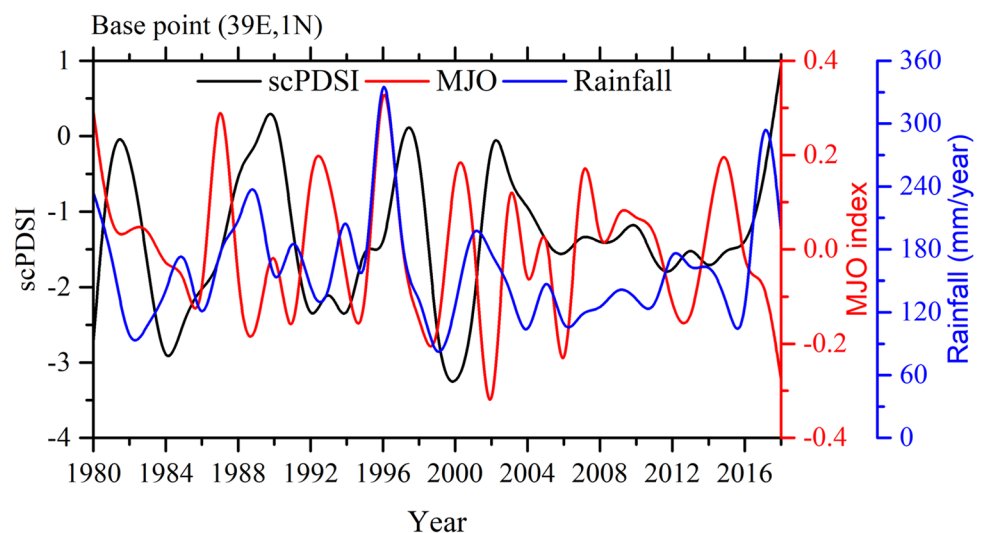
Since CCKWs are embedded within the MJO structure, this may also be similar to MJOs. There may be a halt in the MJO's effect in the middle of the long rainy season, based on the low correlation between MJO indices and Kenyan precipitation. Even if this is the case, our data reveals that the MJO's features change from month to month and decade to decade and that the apparent hiatus may be a product of this variability (Suhas and Goswami 2010).

Research by JunMei et al. 2012 revealed that MJO varies the atmospheric circulation by creating a situation for descending motions that is not favourable for convective activities. MJO phase over the global Ocean basins can alter the Sea Surface Temperatures (SSTs) gradients, consequently changing the teleconnection patterns like the ENSO and IOD (Shimizu and Ambizzi 2016; Shimizu et al. 2017).

4 Conclusion

Droughts and floods have a significant impact on the lives of millions of people in East Africa, delaying progress toward the United Nations Millennium Development Goals. Developing weather and short-term climate forecasting systems to limit the effects of deviations from average weather in the region requires knowledge of variability on intra-seasonal periods. Our results show generally that the influence of MJO on drought variability is seasonally dependent. This influence is visible in the atmospheric circulation patterns and shown by the regression analysis. Thus, the modulation of drought patterns associated with the MJO might somehow regulate the propagation and structure of the atmospheric phenomena responsible for convention such as ENSO, Walker circulation, ITCZ among others.

Even while the impact of MJO on rainfall variability in eastern tropical Africa has long been recognized, no in-depth studies have been conducted on the effects of MJO on abnormalities in atmospheric circulation and extreme weather events. This study addresses this void and establishes the groundwork for a complete and systematic evaluation of the impact on rainfall in Kenya. We used the sc-PDSI index to classify drought events and the convective MJO index filtered from the OLR climate data record to examine how MJOs affect rainfall intensity in Kenya. Both of these indexes were found to be helpful in this study.

Regression analysis (Figs. 8, 9, 10, 11, 12, 13) shows that some eastward migrating signals with wavenumbers 3–8 and periods less than 20 or 25 days also exhibit spatial patterns compatible with the MJO, even though the MJO is generally associated with planetary sizes and periods of 30–60 days (shown in Fig. 4). During MAM and DJF, the MJO contributes a more significant percentage of the variance than during JJA and OND (Fig. 5).

There is a strong correlation between the presence of these cyclones and anticyclones in wind shear structures inside the MJO and their arrival at that place by similar mechanisms (Aiyyer and Molinari 2008; Klotzbach 2014; Schreck 2015). This study has demonstrated that regions of positive shear magnitudes are conducive for the formation of subtropical westerly jet streams, while the negative shear magnitude is associated with easterly jet streams in the tropics. The subtropical westerly jet may be responsible for moisture flux through the advection of the Conga air mass to the east, consequently leading to enhanced rainfall. Likewise, a stronger subtropical easterly Jetstream is conducive to forming strong easterly winds, which leads to an advection of the dry Indian Ocean air mass, causing extreme dry conditions (Finney et al. 2020). The increase of dry extreme events is a matter of grave concern due to the effects on the population and for the survival of the entire ecosystem. MJO influence on rainfall over a given location is phase dependent (Schreck 2015), this was not factored in this study and therefore the drought.

These results of this study can be used to improve drought early warning system by strengthening drought prediction. Further progressive research is needed to understand the linkages between the MJO and drought, and other convective disturbances such as convective Kelvin waves and Rossby waves are, therefore, certainly required based on robust statistical comparisons of their kinematic and thermodynamic structures along with theoretical and simple modelling over the study region.

Declarations

Conflict of interest The authors unilaterally declare no competing interests.

Ethical approval The manuscript was prepared by adhering to the ethical standards of the Meteorology and Atmospheric Physics journal.

Consent to participate Not applicable.

Consent for publication The authors confirm that this research is scientifically founded and consent for it to be published.

References

Aiguo D, Kevin ET, Taotao Q (2004) A global dataset of palmer drought severity index for 1870–2002: relationship with soil moisture and effects of surface warming. J Hydrometeorol 5(6):1117–1130. https://doi.org/10.1016/j.molcel.2017.04.015

Aiyyer A, Molinari J (2008) MJO and tropical cyclogenesis in the Gulf of Mexico and Eastern Pacific: case study and idealized numerical modeling. J Atmos Sci 65(8):2691–2704. https://doi.org/10.1175/2007JAS2348.1

Aiyyer A, Thorncroft C (2011) Interannual-to-multidecadal variability of vertical shear and tropical cyclone activity. J Clim 24(12):2949–2962. https://doi.org/10.1175/2010JCLI3698.1

Ayugi B, Tan G, Ullah W, Boiyo R, Ongoma V (2019) Inter-comparison of remotely sensed precipitation datasets over Kenya during 1998–2016. Atmos Res 225:96–109. https://doi.org/10.1016/j.atmosres.2019.03.032

Ayugi B, Tan G, Rouyun N, Zeyao D, Ojara M, Mumo L, Babaousmail H, Ongoma V (2020) Evaluation of meteorological drought and flood scenarios over Kenya, East Africa. Atmosphere. https://doi.org/10.3390/atmos11030307

Balint Z, Mutua F, Muchiri P, Omuto CT (2013) Monitoring Drought with the Combined Drought Index in Kenya. In: Developments in Earth Surface Processes, 1st ed., vol. 16. Elsevier B.V. https://doi.org/10.1016/B978-0-444-59559-1.00023-2

Basu S, Ramegowda V, Kumar A, Pereira A (2016) Plant adaptation to drought stress. F1000Res 5(F1000 Faculty Rev):1554. https://doi.org/10.12688/F1000RESEARCH.7678.1

Berhane F, Zaitchik B (2014) Modulation of daily precipitation over East Africa by the Madden-Julian oscillation. J Climate 27(15):6016–6034. https://doi.org/10.1175/JCLI-D-13-00693.1

Bond NA, Vecchi GA (2003) The influence of the Madden-Julian oscillation on precipitation in Oregon and Washington. Wea Forecasting 18(4):600–613. https://doi.org/10.1175/1520-0434(2003)018%3c0600:TIOTMO%3e2.0.CO;2

Camberlin P, Janicot S, Poccard I (2001) Seasonality and atmospheric dynamics of the teleconnection between African rainfall and tropical sea-surface temperature: Atlantic vs ENSO. Int J Climatol 21(8):973–1005. https://doi.org/10.1002/joc.673

Dai A (2011) Characteristics and trends in various forms of the palmer drought severity index during 1900–2008. J Geophys Res Atmos. https://doi.org/10.1029/2010JD015541

Dai A (2013) Increasing drought under global warming in observations and models. Nat Clim Change 3(1):52–58. https://doi.org/10.1038/nclimate1633

DeMott CA, Klingaman NP, Woolnough SJ (2015) Atmosphere-ocean coupled processes in the Madden-Julian oscillation. Rev Geophys 53:1099–1154

Dias J, Pauluis O (2009) Convectively coupled waves propagating along an equatorial ITCZ. J Atmos Sci 66(8):2237–2255. https://doi.org/10.1175/2009JAS3020.1

Eichsteller M, Njagi T, Nyukuri E (2022) The role of agriculture in poverty escapes in Kenya–developing a capabilities approach in the context of climate change. World Dev 149:105705. https://doi.org/10.1016/j.worlddev.2021.105705

Ferguson J, Khouider B, Namazi M (2009) Two-way interactions between equatorially-trapped waves and the barotropic flow. Chinese Ann Math Ser B 30(5):539–568. https://doi.org/10.1007/s11401-009-0102-9

Finney DL, Marsham JH, Walker DP, Birch CE, Woodhams BJ, Jackson LS, Hardy S (2020) The effect of westerlies on East African rainfall and the associated role of tropical cyclones and the Madden–Julian Oscillation. Quarterly J Royal Meteorol Soc 146(727):647–664. https://doi.org/10.1002/qj.3698

Frei C, Schöll R, Fukutome S, Schmidli J, Vidale PL (2006) Future change of precipitation extremes in Europe: intercomparison of scenarios from regional climate models. J Geophys Res Atmos 111:D06105. https://doi.org/10.1029/2005JD005965

Funk C (2020) Ethiopia, Somalia and Kenya face devastating drought. Nature 586:645. https://doi.org/10.1038/d41586-020-02698-3

Funk C, Peterson P, Landsfeld M, Pedreros D, Verdin J, Shukla S, Husak G, Rowland J, Harrison L, Hoell A, Michaelsen J (2015) The climate hazards infrared precipitation with stations-a new environmental record for monitoring extremes. Sci Data 2:150066. https://doi.org/10.1038/sdata.2015.66

Gill AE (1980) Some simple solutions for heat-induced tropical circulation. Q J R Meteor Soc 106:447–462

Haile GG, Tang Q, Hosseini-Moghari S-M et al (2020) Projected impacts of climate change on drought patterns over East Africa. Earth's Future. https://doi.org/10.1029/2020EF001502

Harris I, Jones PD, Osborn TJ, Lister DH (2014) Updated high-resolution grids of monthly climatic observations—the CRU TS3.10 dataset. Int J Climatol 34(3):623–642. https://doi.org/10.1002/joc.3711

Hession SL, Moore N (2011) A spatial regression analysis of the influence of topography on monthly rainfall in East Africa. Int J Climatol 31:1440–1456. https://doi.org/10.1002/joc.2174

Hogan E, Shelly A, Xavier P (2015) The observed and modelled influence of the Madden-Julian oscillation on East African rainfall. Meteorol Appl 22(3):459–469. https://doi.org/10.1002/met.1475

Hua L, Ma Z, Zhong LA (2011) A comparative analysis of primary and extreme characteristics of dry or wet status between Asia and North America. Adv Atmos Sci 28(2):352–362. https://doi.org/10.1007/s00376-010-9230-0

Huho MJ, Kosonei RC (2014) Understanding extreme climatic events for economic development in Kenya. IOSR J Environ Sci, Toxicol Food Technol 8(2):14–24. https://doi.org/10.9790/2402-08211424

Indeje M, Semazzi FHM, Ogallo LJ (2000a) ENSO signals in East African rainfall seasons. Int J Climatol 20(1):19–46. https://doi.org/10.1002/(SICI)1097-0088(200001)20:1%3c19::AID-JOC449%3e3.0.CO;2-0

Indeje M, Semazzi FHM, Ogallo LJ (2000b) ENSO signals in East African rainfall seasons. Int J Climatol 46:19–46

IPCC (2022) Climate change 2022: mitigation of climate change. Contribution of working group III to the sixth assessment report of the intergovernmental panel on climate change In: Shukla PR, Skea J, Slade R, Al Khourdajie A, van Diemen R, McCollum D, Pathak M, Some S, Vyas P, Fradera R, Belkacemi R, Hasija A, Lisboa G, Luz S, Malley J (Eds). Cambridge University Press, Cambridge, UK and New York, NY, USA. https://doi.org/10.1017/9781009157926

Junmei LÜ, Jianhua JU, Juzhang REN, Weiwei GAN (2012) The influence of the Madden-Julian Oscillation activity anomalies on Yunnan's extreme drought of 2009–2010. Sci China Earth Sci 55(1):98–112. https://doi.org/10.1007/s11430-011-4348-1

Kikuchi K, Wang B, Kajikawa Y (2012) Bimodal representation of the tropical intraseasonal oscillation. Clim Dyn 38(9–10):1989–2000. https://doi.org/10.1007/s00382-011-1159-1

Kalisa W, Zhang J, Igbawua T, Ujoh F, Ebohon OJ, Namugize JN, Yao F (2020) Spatio-temporal analysis of drought and return periods over the East African region using standardized precipitation index from 1920 to 2016. Agric Water Manag 237:106195. https://doi.org/10.1016/j.agwat.2020.106195

Kanamitsu M, Ebisuzaki W, Woollen J, Yang S, Hnilo JJ, Fiorino M, Potter GL (2002) NCEP–DOE AMIP-II reanalysis (R-2). Bull Amer Meteorol Soc 83(11):1631–1644. https://doi.org/10.1175/BAMS-83-11-1631

Kenyon J, Hegerl GC (2010) Influence of modes of climate variability on global precipitation extremes. J Clim 23:6248–6262

Kiladis GN, Straub KH, Haertel PT (2005) Zonal and vertical structure of the Madden-Julian oscillation. J Atmos Sci 62(8):2790–2809. https://doi.org/10.1175/JAS3520.1

Kilavi M, Macleod D, Ambani M, Robbins J, Dankers R, Graham R, Titley H, Salih AAM, Todd MC (2018) Extreme rainfall and flooding over Central Kenya including Nairobi City during the long-rains season 2018: causes, predictability, and potential for early warning and actions. Atmosphere 9(12):472. https://doi.org/10.3390/atmos9120472

Kimani MW, Hoedjes JCB, Su Z (2017) An assessment of satellite-derived rainfall products relative to ground observations over East Africa. Remote Sens. https://doi.org/10.3390/rs9050430

Kimani M, Hoedjes JCB, Su Z (2020) An assessment of MJO circulation influence on air-sea interactions for improved seasonal rainfall predictions over East Africa. J Clim 33(19):8367–8379. https://doi.org/10.1175/JCLI-D-19-0296.1

Klotzbach PJ (2010) On the Madden-Julian oscillation-atlantic hurricane relationship. J Clim 23(2):282–293. https://doi.org/10.1175/2009JCLI2978.1

Klotzbach PJ (2014) The Madden-Julian oscillation's impacts on worldwide tropical cyclone activity. J Clim 27(6):2317–2330. https://doi.org/10.1175/JCLI-D-13-00483.1

Kossin JP, Camargo SJ, Sitkowski M (2010) Climate modulation of north atlantic hurricane tracks. J Clim 23(11):3057–3076. https://doi.org/10.1175/2010JCLI3497.1

Lanczos C (1950) An interaction method for the solution of the eigenvalue problem of linear differential and integral operators. J Res Natl Bur Stand 45(4):255–282

Le PVV, Phan-Van T, Mai KV, Tran DQ (2019) Space–time variability of drought over Vietnam. Int J Climatol 39(14):5437–5451. https://doi.org/10.1002/joc.6164

Li T (2014) Recent advance in understanding the dynamics of the Madden-Julian oscillation. Acta Meteorol Sin 28:1–33. https://doi.org/10.1007/s13351-014-3087-6

Liebmann B, Smith CA (1996) Description of a complete (interpolated) outgoing longwave radiation dataset. Bull Amer Meteorol Soc 77:1275–1277

Liu L, Hong Y, Bednarczyk CN, Yong B, Shafer MA, Riley R, Hocker JE (2012) Hydro-climatological drought analyses and projections using meteorological and hydrological drought indices: a case study in blue river basin. Oklahoma Water Resour Manag 26(10):2761–2779. https://doi.org/10.1007/s11269-012-0044-y

Lyon B (2014) Seasonal drought in the greater horn of Africa and its recent increase during the March-May long rains. J Climate 27(21):7953–7975. https://doi.org/10.1175/JCLI-D-13-00459.1

Madden RA, Julian PR (1994) Observations of the 40–50-day tropical oscillation—a review. Mon Weather Rev 122:814–837

Masih I, Maskey S, Mussá FEF, Trambauer P (2014) A review of droughts on the African continent: a geospatial and long-term perspective. Hydrol Earth Syst Sci 18(9):3635–3649. https://doi.org/10.5194/hess-18-3635-2014

Masunaga H (2007) Seasonality and regionality of the Madden-Julian oscillation, Kelvin wave, and equatorial Rossby wave. J Atmos Sci 64(12):4400–4416. https://doi.org/10.1175/2007JAS2179.1

Mpelasoka F, Awange JL, Zerihun A (2018) Influence of coupled ocean-atmosphere phenomena on the Greater Horn of Africa droughts and their implications. Sci Total Environ 610–611:691–702. https://doi.org/10.1016/j.scitotenv.2017.08.109

Muller JC-Y (2014) Adapting to climate change and addressing drought–learning from the red cross red crescent experiences in the Horn of Africa. Weather Climate Extremes 3:31–36. https://doi.org/10.1016/j.wace.2014.03.009

Mumo L, Yu J, Fang K (2018) Assessing impacts of seasonal climate variability on Maize Yield in Kenya. Int J Plant Prod 12(4):297–307

Mutai CC, Ward MN (2000) East African rainfall and the tropical circulation/convection on intraseasonal to interannual timescales. J Clim 13:3915–3939

NASA, NIMA, DLR, ASI (2000) SRTM Data Collection. Retrieved October 16, 2021, from https://datasets.wri.org/dataset/kenya-digital-elevation-model-90m-resolution

Ngoma H, Wen W, Ojara M, Ayugi B (2021) Assessing current and future spatiotemporal precipitation variability and trends over Uganda, East Africa, based on CHIRPS and regional climate model datasets. Meteorol Atmos Phys 133(3):823–843. https://doi.org/10.1007/s00703-021-00784-3

Nicholson SE (2018) The ITCZ and the seasonal cycle over equatorial Africa. Bull Amer Meteorol Soc 99(2):337–348

Ochieng P, Nyandega I, Wambua B (2022) Spatial-temporal analysis of historical and projected drought events over Isiolo County. Kenya Theor Appl Climatol 148(1–2):531–550. https://doi.org/10.1007/s00704-022-03953-5

Ogwang BA, Chen H, Tan G, Ongoma V, Ntwali D (2015) Diagnosis of East African climate and the circulation mechanisms associated with extreme wet and dry events: a study based on RegCM4. Arabian J Geosci 8(12):10255–10265. https://doi.org/10.1007/s12517-015-1949-6

Okello P, Guirong T, Ongoma V, Nyandega IA (2021) Influence of convectively coupled equatorial kelvin waves on march-may precipitation over East Africa. Geogr Pannonica 25(1):24–34. https://doi.org/10.5937/gp25-31132

Okoola RE (1999) A diagnostic study of the eastern Africa monsoon circulation during the Northern Hemisphere spring season. Int J Climatol 19(2):143–168. https://doi.org/10.1002/(SICI)1097-0088(199902)19:2%3c143::AID-JOC342%3e3.0.CO;2-U

Omeny PA, Okoola R, Hendon H, Wheeler M (2008) East African rainfall variability associated with the Madden-Julian oscillation. J Kenya Meteorol Soc 2(2):105–114

Omondi PA, Awange JL, Forootan E, Ogallo A, Girmaw B, Fesseha I, Kululetera V, Mbati M, Kilavi M, King M, Adek P, Njogu A, Badr M, Musa A, Muchiri P (2014) Changes in temperature and precipitation extremes over the Greater Horn of Africa region from 1961 to 2010. Int J Climatol 34:1262–1277. https://doi.org/10.1002/joc.3763

Ongoma V, Chen H (2017) Temporal and spatial variability of temperature and precipitation over East Africa from 1951 to 2010. Meteorol Atmos Phys 129:131–144. https://doi.org/10.1007/s00703-016-0462-0

Ongoma V, Guirong T, Ogwang B, Ngarukiyimana J (2015) Diagnosis of seasonal rainfall variability over east africa: a case study of 2010–2011 drought over Kenya. Pakistan J Meteorol 11(22):13–21

Ongoma V, Chen H, Gao C, Nyongesa AM, Polong F (2018) Future changes in climate extremes over Equatorial East Africa based on CMIP5 multimodel ensemble. Nat Hazards 90(2):901–920. https://doi.org/10.1007/s11069-017-3079-9

Owiti Z, Ogalo L (2014) Linkages between the Indian Ocean Dipole and East African Rainfall Anomalies Linkages between the Indian Ocean Dipole and East African Seasonal Rainfall Anomalies. July, 2–17

Owiti Z, Ogallo L, Mutemi J (2008) Linkages between the Indian Ocean Dipole and east African seasonal rainfall anomalies. J Kenya Meteorol Soc 2(2): 2–17. www.kenyamet.org

Palmer WC (1965) Meteorological Drought. In U.S. Weather Bureau, Res. Pap. No. 45 (p. 58). https://www.ncdc.noaa.gov/temp-and-precip/drought/docs/palmer.pdf

Pohl B, Camberlin P (2006) Influence of the Madden-Julian oscillation on East African rainfall. I: intraseasonal variability and regional dependency. Q J R Meteorol Soc 132(621):2521–2539. https://doi.org/10.1256/qj.05.104

Pohl B, Camberlin P (2014) A typology for intraseasonal oscillations. Int J Climatol 34:430–445

Pohl B, Matthews AJ (2007) Observed changes in the lifetime and amplitude of the Madden-Julian oscillation associated with interannual ENSO sea surface temperature anomalies. J Clim 20:2659–2674

Polong F, Chen H, Sun S, Ongoma V (2019) Temporal and spatial evolution of the standard precipitation evapotranspiration index (SPEI) in the Tana River Basin. Kenya Theor Appl Climatol 138(1–2):777–792. https://doi.org/10.1007/s00704-019-02858-0

Roundy PE (2008) Analysis of convectively coupled Kelvin waves in the Indian ocean MJO. J Atmos Sci 65(4):1342–1359. https://doi.org/10.1175/2007JAS2345.1

Roundy PE (2012) The spectrum of convectively coupled Kelvin waves and the Madden-Julian oscillation in regions of low-level easterly and westerly background flow. J Atmos Sci 69(7):2107–2111. https://doi.org/10.1175/JAS-D-12-060.1

Roundy PE (2014) Regression analysis of zonally narrow components of the MJO. J Atmos Sci 71(11):4253–4275. https://doi.org/10.1175/JAS-D-13-0288.1

Roundy PE (2018) A wave-number frequency wavelet analysis of convectively coupled equatorial waves and the MJO over the Indian Ocean. QJR Meteorol Soc 144(711):333–343. https://doi.org/10.1002/qj.3207

Roundy PE, Frank WM (2004) A climatology of waves in the equatorial region. J Atmos Sci 61(17):2105–2132. https://doi.org/10.1175/1520-0469(2004)061%3c2105:ACOWIT%3e2.0.CO;2

Roundy PE, Schreck CJ, Janiga MA (2009) Contributions of convectively coupled equatorial Rossby waves and Kelvin waves to the real-time multivariate MJO indices. Mon Weather Rev 137(1):469–478. https://doi.org/10.1175/2008MWR2595.1

Schreck CJ (2015) Kelvin waves and tropical cyclogenesis: A global survey. Mon Weather Rev 143(10):3996–4011. https://doi.org/10.1175/MWR-D-15-0111.1

Schreck CJ (2021) Global survey of the MJO and extreme precipitation. Geophys Res Lett. https://doi.org/10.1029/2021GL094691

Schreck CJ, Shi L, Kossin JP, Bates JJ (2013) Identifying the MJO, equatorial waves, and their impacts using 32 years of HIRS upper-tropospheric water vapor. J Clim 26(4):1418–1431. https://doi.org/10.1175/JCLI-D-12-00034.1

Seneviratne SI, Nicholls N, Easterling D, Goodess CM, Kanae S, Kossin J, et al (2012) Changes in climate extremes and their impacts on the natural physical environment. Managing the Risks of Extreme Events and Disasters to Advance Climate Change Adaptation: Special Report of the Intergovernmental Panel on Climate Change, pp 109–230. https://doi.org/10.1017/CBO9781139177245.006

Shanko D, Camberlin P (1998) The effects of the southwest Indian ocean tropical cyclones on Ethiopian drought. Int J Climatol 18(12):1373–1388. https://doi.org/10.1002/(SICI)1097-0088(1998100)18:12%3c1373::AID-JOC313%3e3.0.CO;2-K

Shimizu MH, Ambrizzi T (2016) MJO influence on ENSO effects in precipitation and temperature over South America. Theor Appl Climatol 124(1–2):291–301. https://doi.org/10.1007/s00704-015-1421-2

Shimizu MH, Ambrizzi T, Liebmann B (2017) Extreme precipitation events and their relationship with ENSO and MJO phases over northern South America. Int J Climatol 37(6):2977–2989. https://doi.org/10.1002/joc.4893

Suhas E, Goswami BN (2010) Loss of significance and multidecadal variability of the Madden-Julian oscillation. J Clim 23(13):3739–3751. https://doi.org/10.1175/2010JCLI3180.1

Sun Q, Miao C, AghaKouchak A, Duan Q (2016) Century-scale causal relationships between global dry/wet conditions and the state of the Pacific and Atlantic Oceans. Geophys Res Lett 43:6528–6537

Trenberth K, Dai A, van der Schrier G et al (2014) Global warming and changes in drought. Nature Clim Change 4:17–22. https://doi.org/10.1038/nclimate2067

Ventrice MJ, Wheeler MC, Hendon HH, Schreck CJ, Thorncroft CD, Kiladis GN (2013) A modified multivariate Madden-Julian oscillation index using velocity potential. Mon Weather Rev 141(12):4197–4210. https://doi.org/10.1175/MWR-D-12-00327.1

Vicente-Serrano SM (2005) El Niño and La Niña influence on droughts at different timescales in the Iberian Peninsula. Water Resour Res 41:W12415. https://doi.org/10.1029/2004WR003908

Wang L, Chen W, Zhou W, Huang G (2015) Teleconnected influence of tropical Northwest Pacific Sea surface temperature on interannual variability of autumn precipitation in Southwest China. Clim Dyn 45(9–10):2527–2539. https://doi.org/10.1007/s00382-015-2490-8

Weisheimer A, Schaller N, O'Reilly C, MacLeod DA, Palmer T (2017) Atmospheric seasonal forecasts of the twentieth century: multidecadal variability in predictive skill of the winter North Atlantic Oscillation (NAO) and their potential value for extreme event attribution. Q J R Meteorol Soc 143:917–926

Wells N, Goddard S, Hayes MJ (2004) A self-calibrating palmer drought severity index. J Clim 17(12):2335–2351. https://doi.org/10.1175/1520-0442(2004)017

Wheeler M, Kiladis GN (1999) Convectively coupled equatorial waves: analysis of clouds and temperature in the wavenumber-frequency domain. J Atmos Sci 56(3):374–399. https://doi.org/10.1175/1520-0469(1999)056%3c0374:CCEWAO%3e2.0.CO;2

Wilson EA, Gordon AL, Kim D (2013) Observations of the madden julian oscillation during Indian ocean dipole events. J Geophys Res Atmos 118(6):2588–2599. https://doi.org/10.1002/jgrd.50241

Yang SE, Wu BF (2010) Calculation of monthly precipitation anomaly percentage using web-serviced remote sensing data. In: Proceedings - 2nd IEEE International Conference on Advanced Computer Control, ICACC 2010, vol 5, pp 621–625. https://doi.org/10.1109/ICACC.2010.5486796

Yevjevich V (1969) An objective approach to definitions and investigations of continental hydrologic droughts. J Hydrol 7(3):353. https://doi.org/10.1016/0022-1694(69)90110-3

Zhang C (2005) Madden-Julian oscillation. Rev Geophys. https://doi.org/10.1029/2004RG000158

Zhang X, Wang J, Zwiers FW, Groisman PY (2010) The influence of large-scale climate variability on winter maximum daily precipitation over North America. J Clim 23:2902–2915